The accretion history of the Milky Way IV. Hints of recent star formation in Milky Way dwarf spheroidal galaxies

Yanbin Yang^{1,*}, Elisabetta Caffau¹, Piercarlo Bonifacio¹, François Hammer¹, Jianling Wang², and Gary A. Mamon³

- ¹ GEPI, Observatoire de Paris, Université PSL, CNRS, Place Jules Janssen, 92190 Meudon, France
- CAS Key Laboratory of Optical Astronomy, National Astronomical Observatories, Beijing 100101, China
- Institut d'Astrophysique de Paris (UMR7095: CNRS & Sorbonne Université), 98 bis Bd Arago, 75014, Paris, France

ABSTRACT

ABST

Owarf spheroidal galaxies are known to be dominated by old stel progenitors lost their gas during their infall in the Milky Way (M' a tiny but robustly detected population of possibly young (~ 1 G dwarf spheroidal galaxies. This was established on the basis of their of the foreground MW using Gaia DR3 proper motions. We have blue stragglers. For Sculptor, it seems unlikely, because 95.5% of M_☉. This would only allow blue straggler masses of less than 1.8 would require the merger of three turnoff stars, which appears eve measurements of MW dwarf galaxies infer their low binding energinfall. Although the nature of the newly discovered stars still net recent infall of the dwarf galaxies into the MW halo, when star fe before its removal by the hot Galactic corona. The abundance of the drawn from hydrodynamical simulations. These results point to a late of the Milky Way (MW) during a process of gas loss due to ram pressure stripping exerted by the Galactic hot corona. This also provides a reasonable explanation of the morphology density relation (Putman et al. 2021), whereby dwarfs inside (outside) 250 kpc from their MW or M31 host are mostly gas-free and dispersion supported (gas-rich and rotation-supported) systems, respectively.

However, the infall time of most MW dwarfs (those within ~ 250 kpc) is still a matter of debate. For a long time, it was accepted that the cutoff of dwarf star formation history (SFH) provides a good clock to estimate their infall time. This argument is mostly limited to classical dwarf spheroidal galaxies (dSphs) for which the stellar population (especially of the red-giant branch, RGB) is sufficiently abundant to retrieve the SCHL. Heads to extensive resorted to the reinfall abundant to retrieve the SCHL. Heads to extensive for instance, Scalatae the start of the stellar population (especially of the red-giant branch, RGB) is sufficiently abundant to retrieve Dwarf spheroidal galaxies are known to be dominated by old stellar populations. This has led to the assumption that their gas-rich progenitors lost their gas during their infall in the Milky Way (MW) halo at distant look-back times. Here, we report a discovery of a tiny but robustly detected population of possibly young (~ 1 Gyr old) and intermediate-mass $(1.8 M_{\odot} \le M < 3 M_{\odot})$ stars in MW dwarf spheroidal galaxies. This was established on the basis of their positions in color-magnitude diagrams, after filtering out the bulk of the foreground MW using Gaia DR3 proper motions. We have considered the possibility that this population is made of evolved blue stragglers. For Sculptor, it seems unlikely, because 95.5% of its stars are older than 8 Gyr, leading to masses smaller than 0.9 M_{\odot} . This would only allow blue straggler masses of less than 1.8 M_{\odot} , which is much lower than what we observed. Alternatively, it would require the merger of three turnoff stars, which appears even more unlikely. On the other hand, the recent Gaia proper motion measurements of MW dwarf galaxies infer their low binding energies and large angular momenta, pointing to a more recent, ≤ 3 Gyr, infall. Although the nature of the newly discovered stars still needs further confirmation, we find that they are consistent with the recent infall of the dwarf galaxies into the MW halo, when star formation occurred from the ram pressurization of their gas content before its removal by the hot Galactic corona. The abundance of this plausibly young population of stars is similar to the expectations drawn from hydrodynamical simulations. These results point to a novel origin for MW dwarf spheroidal galaxies.

Key words. galaxies: abundances – galaxies: dwarf – galaxies: star formation

galaxies (dSphs) for which the stellar population (especially of the red-giant branch, RGB) is sufficiently abundant to retrieve their SFHs. It leads to contrasting results; for instance, Sculptor (De Boer et al. 2012a), Ursa Minor, Sextans (Bettinelli et al. 2018; Lee et al. 2009; Carrera et al. 2002), and Draco (Mapelli et al. 2007) showed a sharp decrease of their SFHs 8 to 10 Gyr ago. Meanwhile, Fornax (Saviane et al. 2000; De Boer et al. 2012b), Carina (De Boer et al. 2014; Monelli et al. 2003; Weisz et al. 2014), and Leo I (Ruiz-Lara et al. 2021) showed extended SFHs including toward very recent epochs (0.1 to 2 Gyr ago).

Intermediate-to-young stars have been detected in the central region of LeoII (Komiyama et al. 2007). Canes Venatici I, having a stellar mass similar to that of Carina and of UMi, also shows star formation activity about 1.5–2 Gyr ago (Weisz et al. 2014; Martin et al. 2008).

Concerning more in-depth studies of stellar population, the notion that dSphs are mainly made up of old stars has been met with a broad consensus, based on a clearly defined turnoff (TO) of an old population, visible in the color-magnitude diagrams (CMDs) of all dSphs (see Tolstoy et al. 2009, and references therein). The possible presence of a young population in dSph galaxies, on the other hand, is highly controversial. For example, while there is a consensus on the dominance of an old population in the Draco dSph, Aparicio et al. (2001) claimed the detection of a young population of 2-3 Gyr. On the other hand, Mapelli et al. (2007) provided circumstantial evidence (mainly based on the spatial distribution of "blue plume," BP, stars) of an absence of young populations; in addition, these authors posited that BPs are indeed blue straggler stars (hereafter, BSSs), although they clearly mention that the presence of a young population suggested by Aparicio et al. (2001) cannot be ruled out. The claims of a young population in dSph galaxies hinge on the ubiquitous "blue plumes" (BP) observed in the CMDs of all dSph galaxies (see Momany et al. 2007; Santana et al. 2013). These BP stars appear as an extension to the blue of the main sequence (MS), beyond the TO of the old population.

^{*} E-mail: yanbin.yang@obspm.fr

The claims of the existence of young populations have also been based on another feature often seen in CMDs: a vertical sequence of stars bluer than the RGB, which extends (in certain cases) to magnitudes brighter than the horizontal branch (HB). This sequence is usually called the "vertical clump" (VC, Gallart et al. 2005) or "yellow plume" (e.g., Gullieuszik et al. 2008) or even "blue loop" (De Boer et al. 2012a). The location of this vertical sequence of blue stars in the CMD is consistent with stars of mass in the range $1.5 \le M/M_{\odot} \le 4$ and ages younger than 4 Gyr, in the phase of core-helium burning (CHeB). We refer to these stars as CHeBs, although some sub-giants stars in the same mass range, can occupy the same region in the CMD. The interpretation of these features in CMDs is ambiguous: while the BP and the CHeB can be interpreted as MS and CHeB phases of a young population, they can also be interpreted as BSSs and evolved BSSs (in the CHeB phase).

The above discussion leads to some ambiguity on the SFH of dSphs, and, thus, their related infall times. However, the accurate proper motions of the MW dSphs from the Gaia EDR3 (Li et al. 2021; Battaglia et al. 2022) have revolutionized our understanding of the dSph orbital motions, providing accurate values of orbital energies for a given MW mass model. In the accepted hierarchical scenario of structure formation, the most recent newcomers typically have smaller binding energies than satellites that entered at early epochs (Gott 1975). Such a behavior has been confirmed with cosmological simulations (Rocha et al. 2012; Santistevan et al. 2023), demonstrating a tight correlation between the infall lookback time and the binding energy. D'Souza & Bell (2022) retrieved the same correlation for most of the simulated halos of the ELVIS suite (Garrison-Kimmel et al. 2014), finding it was corrupted in only 3 of 48 halos having a very active merger history, which unlikely applies to the relatively quiet MW (Hammer et al. 2007). In particular, Hammer et al. (2023, hereafter Paper I, see their Fig. 6) confirmed this relationship for the MW, using the globular clusters associated to the bulge, as well as those associated with the Kraken, Gaia-Sausage-Enceladus (GSE), and Sgr, which merged with the MW early on. The latter events are associated to much larger binding energies than that of dSphs. In other words, events that took place 8-10 (GSE) and 4-6 (Sgr) Gyr ago, are six and three times more bound than dSphs, respectively. Paper I presented the conclusion that MW dSphs are likely newcomers, arriving into the MW halo during the past 3 Gyr. The main advantage of the above approach is that it does not depend on the assumed total mass value of the MW, since it is only based on the energy difference with well-known events (Kraken, GSE, and Sgr). Other studies based on Gaia proper motions (Fritz et al. 2019; Battaglia et al. 2022) may offer different conclusions, depending on their assumed choice for the MW mass (see a discussion in Li et al. 2021), which is also an important matter of debate (Jiao et al. 2023; Ou et al. 2024).

A timescale of \leq 3 Gyr is too short for MW dSphs to make more than one orbit because they lie at large distances. For most of them, they would be at their first entry in the MW halo, similar to the Magellanic Clouds (MCs, Kallivayalil et al. 2013). A recent infall history for dSphs means that they may have been gas-rich less than 3 Gyr ago, as are the dwarf irregulars that dominate the dwarf population of the Local Group at distances greater than 250 kpc from the MW or M31 (see e.g., Grcevich & Putman 2009; Putman et al. 2021). Ram pressure stripping of their gas by the hot gas corona of the MW is understood

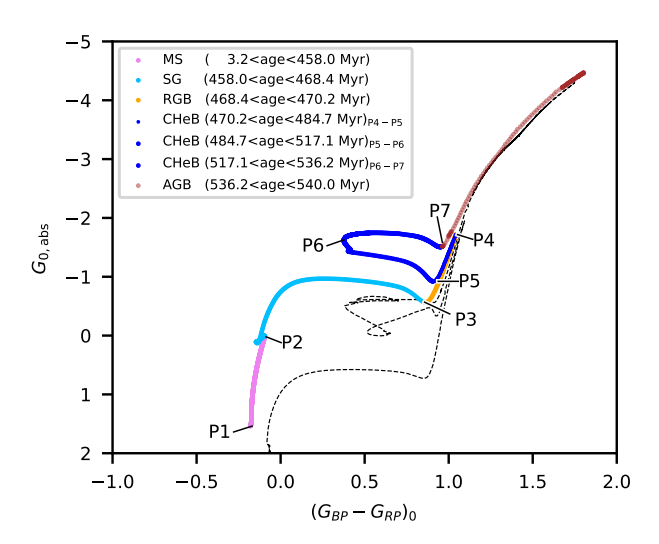


Fig. 1. Example of the PARSEC evolutionary track of an intermediate-mass star ($m=2.4M_{\odot}$ and [Fe/H] = -1.30) in the photometric system of *Gaia*. Numbers P1–7 correspond to the starting point of each evolutionary phase encoded by colors, as explained in the legend (together with the age interval of each phase indicated). The subscript "0" in the axis labels denotes that no reddening has been applied. The dashed line represents an evolutionary track (within 665 Myr) of a BSS of 1.57 M_{\odot} and [Fe/H]= -2.3, which is formed by the merger of two MS stars of $0.8~M_{\odot}$ (Sills et al. 2009).

to have caused their transformation into dSphs (e.g., Mayer et al. 2006; Yang et al. 2014), to which we should add the impact of tidal shocks (Aguilar et al. 1988; Hammer et al. 2024, hereafter Paper II). This mechanism has been explored by Wang et al. (2024, hereafter Paper III), who used hydrodynamical simulations to successfully reproduce the morphologies, internal kinematics, and orbital properties of, for instance, Sculptor. If dSphs fell into MW within the last 3 Gyr as proposed in Paper I, the transformation from dIrrs to dSphs would have occurred rapidly and violently (see Paper III). In particular, gas is expected to be compressed before its removal, leading to the formation of young stars (Bothun & Dressler 1986), whose (small) fraction is predicted in Paper III.

The goal of this paper is to verify whether or not there is a population of young, less than 3 Gyr-old stars, in the dSphs but Sgr. The main text focuses on the Sculptor dSph properties, while most properties of other dSphs are presented in the Appendices. In Sect. 2, we describe our strategy to identify young stellar population in the dSphs. In Sect. 3, we describe the analysis and results based on the *Gaia* photometry. Section 4 presents the analysis of a spectroscopic sample of Sculptor stars. Our discussion and conclusion are given in Sect. 5 and 6, respectively.

2. Methodology

The MS stars that are most proliferous in number would be the ideal stellar population for probing recent star formation. However, to study the MS star in dSphs is very difficult because of their mix with BSSs in the BP region of the CMD. As an alternative probe of recent star formation, we propose investigating intermediate-mass stars (between 1.5 to 8 M_{\odot}) when they are in the sub-giant (SG) phase and the CHeB phase. In Figure 1, we show a PARSEC stellar evolutionary track (Bressan et al. 2012) of an intermediate-mass star. We may notice that after leaving

the main sequence (P1–P2), the star rapidly passes through the SG phase (P2–P3) on a Kelvin-Helmholtz or thermal time scale (10 Myr here), and then enters the RG phase at P3. At the tip of RGB (P4), it ignites helium burning in the core, when phases P4 to P7 cause the star to perform a "blue loop" in the CMD, before reaching the asymptotic giant branch (AGB) phase (P7). All phases before P7 take 536 Myr, which include almost 90% of the time in the MS and about 10% in the SG and the CHeB phases. Depending on the mass, age, and metallicity of stars, the shape of the blue loop changes considerably over a wide region of CMD. When considering all evolutionary tracks of intermediate-mass stars, the CHeB phases overlap with part of the SG phases in CMD and occupy the region above the HB of the old stellar population and bluer than the RGB stars. The CHeB phase may last for a few tens of Myr, depending on the masses and metallicities of stars.

CHeB stars are young, of typically less than 2 Gyr. For example, the Classical Cepheids are the stars in CHeB phase when they are crossing the instability strip (Christy 1966; Fernie 1990; Maran 1991). In most of the dSphs, a handful sample of Anomalous Cepheid (AC) has been noticed (Mateo et al. 1998; Kinemuchi et al. 2008; Monelli & Fiorentino 2022; Soszyński et al. 2020, and references therein). On the other hand, it is unclear whether they are young stars or rejuvenated stars that were formed by binaries (i.e., evolved BSSs).

To identify the full CHeB population in dSphs is challenging because there are not many of them and they can be highly contaminated by foreground MW stars due their locations in the CMD (see e.g., De Boer et al. 2011). Here, we propose a different approach to select CHeB stars in MW dSphs by using the Gaia data. Since the dSphs are moving differently from most of the MW stars, we may use proper motion (PM) to distinguish their stars from those belonging to the MW. We may call this technique "PM-filter," as adopted by Yang et al. (2022). These authors were able to suppress the MW contamination down to a level of 0.1% in the Fornax dSph field of view. This allows to reach a background of contamination 100 times smaller than ground-based observations, which is very useful for deriving the density profile of dSphs, including Fornax. The use of PM for membership selection in dwarf galaxies and clusters is not new (see e.g., Eskridge & Schweitzer 2001), but the quantity and quality of PMs provided by Gaia, with respect to what was available from ground-based observations, makes it much more powerful and precise. CHeB stars in some of the MW dSphs are brighter than 20 mag in the Gaia G-band. Thus, the removal of the foreground MW stars is expected to be efficient thanks to the high quality data of Gaia.

Furthermore, the spectroscopic confirmation of CHeB candidates is helpful to confirm their membership, as well as to provide metallicity in order to resolve the degeneracy between mass, age, and metallicity. Here, we have chosen Sculptor as the best target to perform spectroscopic analysis for CHeB candidates, because spectra for these stars are available in the ESO archive. Sculptor is often considered as an archetype for an old dSph, without significant star formation in the past 5-7 Gyr (De Boer et al. 2012a).

3. Search for CHeB populations in dSphs

3.1. Gaia EDR3 and PM-selected member sample of dSphs

In this subsection we focus in identifying dSph stars using a selection from their PMs using *Gaia* EDR3 data. Our study focuses on the classical dSphs listed in Table 1. We have

excluded Leo I, and Leo II because they are too far to be reached by Gaia for our analysis. Sgr has been also removed since it has a very different infall history compared to other classical dSphs (see, e.g., Paper I). For each dSph we have downloaded all Gaia data within a 10-degree radius from the main table of the Gaia EDR3 archive¹, with the combination of the following conditions: 1) not duplicated_source; 2) not QSO; 3) with color bp_rp measured; 4) with astrometric solutions (either five parameters or six parameters); 5) G < 20.8; 6) ruwe < 1.4; and 7) $C^* < 1.0$. Here, C^* is the corrected phot_bp_rp_excess_factor introduced by Riello et al. (2021), which is efficient for removing background galaxies using the condition we adopted here (see their Figure 21). To exclude QSOs, we used the sample provided by the Gaia EDR3; namely, the table gaiaedr3.agn_cross_id.

Following the method introduced by Yang et al. (2022), as well as their coordinate definition centered on object, we applied the PM-filter to the *Gaia* data and obtained a "PM-selected" sample for each dSph. Below, we provide a detailed description for the Sculptor dSph. We have also derived their morphological parameters, such as the position angle (PA) and ellipticity, *e*, which are listed in Table 1.

Here, we briefly describe the algorithms (see also Sect. 4.1 in Yang et al. 2022) we used to obtain the proper-motion (PM)-selected sample for Sculptor star members. The same methodology has been applied for other dSph star members. First, we examine the proper motion distribution of the raw *Gaia* data, by defining an object-sample and a control-sample, as shown in Figure 2 (a).

The proper motion distributions of both the object-sample and the control-sample are shown in Figure 2 (b) and (c), respectively. The object-sample primarily consists of the member stars of Sculptor. Thus, the concentration of proper motion in Figure 2 (b) is dominated by the member stars of Sculptor. The dispersion in a elliptical shape of the concentration reflects the uncertainty of proper motions, and the correlation between μ_x and μ_y , respectively. By fitting the PM distribution of the object-sample, we obtained a black ellipse (as plotted in the panel) that encloses most of the member stars of Sculptor. It defines our selection region of member candidates in PM space.

We could improve the selection by defining a member candidate when its proper motion is consistent with the mean proper motion of Sculptor, within a tolerance of three times its own uncertainty. The later condition takes into account the fact that the uncertainties in the proper motions change with the magnitude of the sources. Therefore, brighter MW sources with better accuracy could be easily eliminated, as a result of the proper motion selection (i.e., the PM-filter).

Our primary goal is to search for unknown stellar population in dSphs. Thus, our method is relatively simple without assuming priors in colours of stars and their spatial distribution as adopted in the likelihood algorithm by Pace & Li (2019), see also McConnachie & Venn (2020) and Battaglia et al. (2022). Our choice avoids any possible bias at the price of accepting a certain level of non-member contamination, which can, however, be evaluated in the subsequent analysis.

Figure 2 (d) illustrates how efficiently the PM-filter eliminates contamination. It displays a subset of the control-sample in an annulus ranging from radii of 4.0 to 4.02 degrees, which covers the same sky area as the object-sample does. Therefore, Fig-

¹ Gaia Archive at https://gea.esac.esa.int/archive/

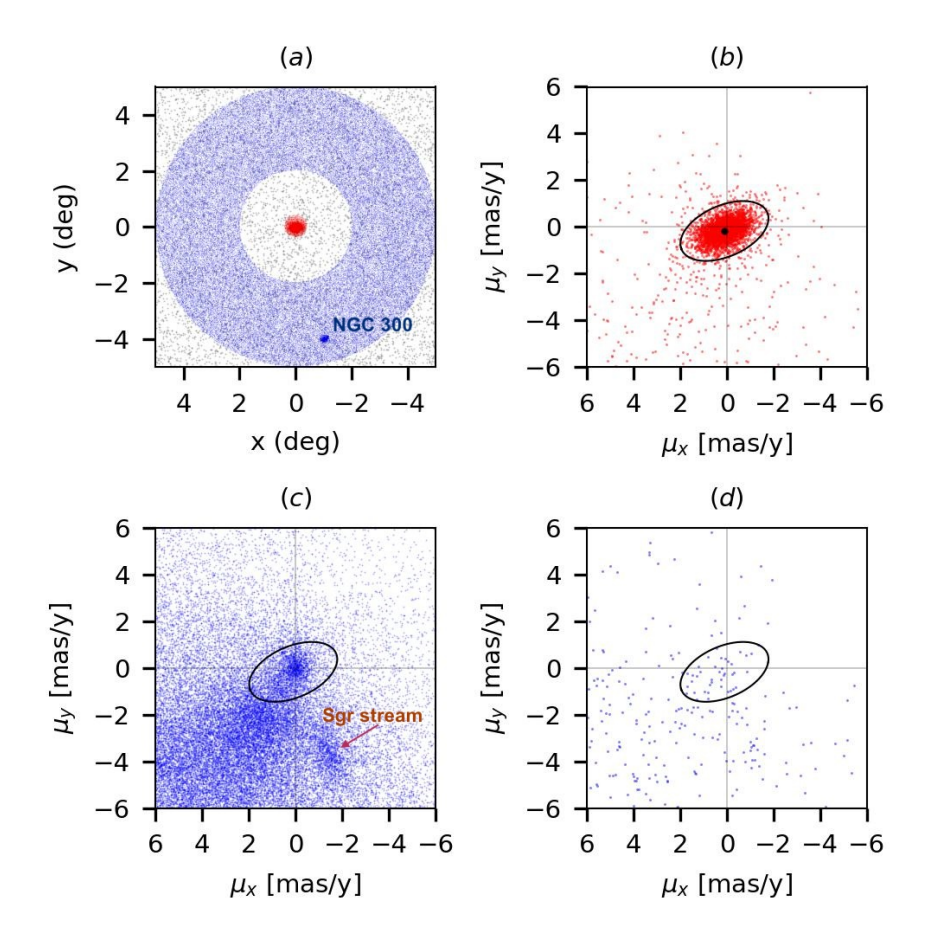


Fig. 2. Diagnosis of the PM distribution of stars in the field centered on Sculptor. Panel (a) shows the spatial distribution of all Gaia sources (gray dots) in a 5×5 sq degree field of view, centered on Sculptor. Among these Gaia sources, we defined an object-sample (red dots) by selecting all sources within a circle of 0.4degree radius and a control-sample (blue dots) by selecting all sources within an annulus from 2 to 5 degrees. Panel (b) gives the proper motion distribution of the object-sample. Panel (c) provides the proper motion distribution of the control-sample. In panels (b), (c), and (d), the black eclipse (with a major-axis radius of 2.0 mas/yr) indicates the maximal region of our proper motion selection of Sculptor member candidates. To illustrate the MW contamination inside the black ellipse, panel (d) shows the proper motion distribution of a sub-controlsample within an annulus from 4.0 to 4.02 degrees, which covers the same sky area as the black ellipse.

ure 2(d) illustrates that the level of contamination in the object-sample is small (0.7%).

3.2. Preparation of PARSEC evolutionary tracks and BaSTI

We used PARSEC stellar evolutionary tracks² and isochrones³ as the reference to identify CHeB star candidates, as well as to study their stellar parameters. Using the YBC database of stellar bolometric corrections (Chen et al. 2019), we have computed magnitudes and colors in the *Gaia* photometric system; namely, G, G_{BP} , and G_{RP} including Galactic extinction for all PARSEC tracks. We prefer to "redden" the theoretical tracks, rather than "de-redden" the observed photometry, because the extinction coefficients depend on effective temperature and gravity of the tracks. While these are perfectly well-known for the theoretical tracks, they are not so for the observed stars. For each dSph, we computed the magnitudes and colors, according to its Galactic extinction (Table 1) for a full set of PARSEC evolutionary tracks. In the following analysis, when we mention evolutionary tracks, we implicitly refer to the track library dedicated to the corresponding dSph.

In the discussion, we also used BaSTI⁴ (Pietrinferni et al. 2024, 2021; Hidalgo et al. 2018) to simulate synthetic CMD in order discuss the stellar population of dSphs. Although BaSTI is based on a stellar evolutionary library different from PARSEC, for our discussion of stellar population this has a marginal im-

pact because synthetic CMD is more related to the star formation history of dSphs and the initial mass function (IMF) of star formation.

3.3. CHeB candidates in dSphs

In the following we will concentrate on the analysis of CHeB stars lying in the Sculptor dSph, although the same methodology applies to other dSphs. Results for the latter galaxies are presented in Appendices A and B.

3.3.1. Step 1: The selection of CHeB population.

Figure 3 shows the CMD of Sculptor and compares it to PAR-SEC evolutionary tracks. The right panel identifies stars older than 7 Gyr on the basis of evolutionary tracks for stellar mass larger than 0.1 M_{\odot} , and within the Sculptor's metallicity range in Table 1. The limit of 7 Gyr corresponds to the dominant stellar population according to De Boer et al. (2012a). Similarly, we have indicated a 2-Gyr limit for RGB stars, which is indicated by the red dashed line. We may notice that Sculptor may have some stars formed in between the past 2 to 7 Gyr, although these stars would be more difficult to identify without ambiguity due to photometric errors on colours and the limited colour spread of RGBs that encompass this range of ages. In the left panel of Figure 3, we superposed all evolutionary tracks for stellar ages smaller than 2 Gyr, within the Sculptor's metallicity range (Table 1), and within a mass range of [1.8 to 3.0] M_{\odot} . Stars bluer than the 2-Gyr limit and well above the HB are consistent with intermediate-mass stars in the CHeB phase. Of course, we could argue these stars could be also rejuvenated stars that were formed

² https://people.sissa.it/~sbressan/CAF09_V1.2S_M36_

³ CMD 3.7 at http://stev.oapd.inaf.it/cgi-bin/cmd_3.7

⁴ http://basti-iac.oa-teramo.inaf.it/syncmd.html

Table 1. Parameters of dSphs

	(1)	(2)	(3)	(4)	(5)	(6)
Name	$(m - M_0)$	E(B-V)	[Fe/H]	PA	e	$r_{ m half}$
				(deg)		(deg; kpc)
Sculptor	19.67 ± 0.13	0.0135 ± 0.0013	(-2.5, -0.8)	95.4	0.28	0.205; 0.308
Sextans	19.89 ± 0.07	0.0449 ± 0.0046	(-3.0, -0.7)	51.1	0.55	0.290; 0.382
UMi	19.4 ± 0.11	0.0283 ± 0.0047	(-3.5, -0.7)	88.0	0.32	0.166; 0.240
Draco	19.57 ± 0.16	0.0290 ± 0.0028	(-3.0, -0.8)	30.5	0.12	0.295; 0.433
Carina	20.13 ± 0.10	0.0600 ± 0.0075	(-3.5, -0.4)	61.1	0.31	0.191; 0.353
Fornax	20.72 ± 0.05	0.0251 ± 0.0041	(-2.8, 0.0)	47.3	0.32	0.307; 0.745

Column-(1): Distance modulus from Li et al. (2021) and references therein.

Column-(2): Galactic extinction, that are calculated by averaging the extinction map within 1 degree around each object, based on the map by Schlegel et al. (1998) via https://irsa.ipac.caltech.edu/applications/DUST/.

Column-(3): Metallicity range, which are taken from Kirby et al. (2011), except for Carina (from Koch et al. (2006)).

Column-(4-6): Morphological parameters: Position Angle (PA), ellipticity (e), half-light radius, respectively. We adopted e = 1 - b/a, where a and b are the major and minor radius, respectively. PA and e have been calculated from our PM-selected sample and r_{half} values have been taken from Muñoz et al. (2018).

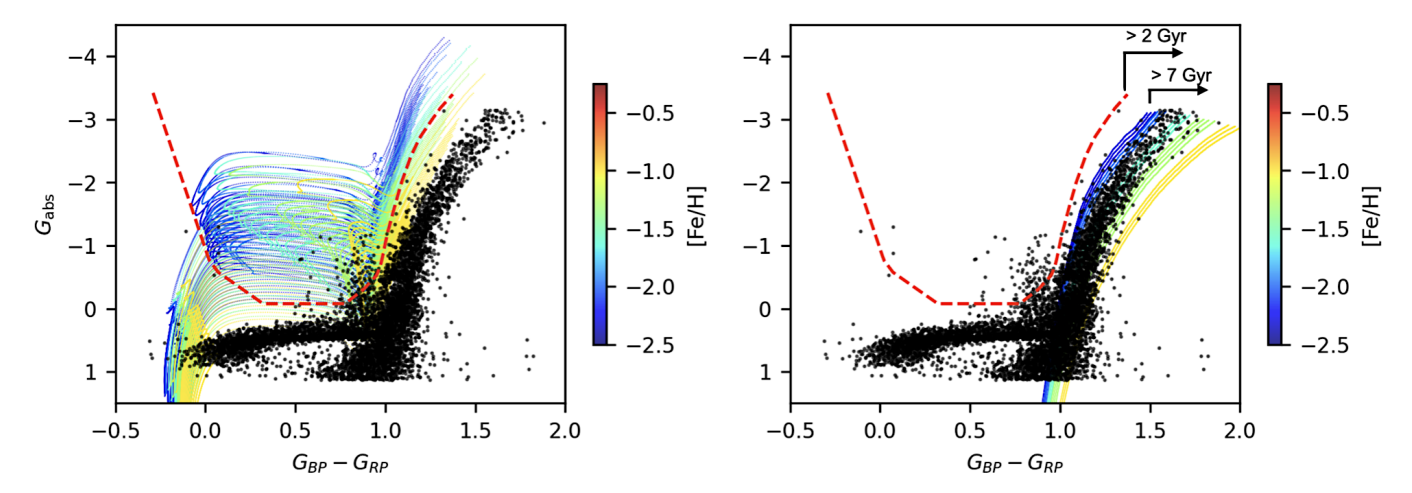


Fig. 3. Sculptor stars (black points) in the CMD based absolute G_{abs} magnitudes and $G_{BP} - G_{RP}$ colors. The sample is selected from a region of 1.1-degree elliptical radius. In both panels, PARSEC stellar evolutionary tracks are overlaid with color coding for the corresponding [Fe/H] of the tracks, and the red dashed line describes our selection condition for CHeB candidates (see Sect. 3.3.1). Left: We superposed all points of evolutionary tracks with the following conditions: stars younger than 2 Gyr, with [Fe/H] ranging from -2.5 to -0.8, and with masses between 1.8 and 3.0 M_{\odot} . Right: We superposed all points of the evolutionary tracks with the following conditions: stars older than 7 Gyr, with [Fe/H] ranging from -2.5 to -0.8, and with masses above 0.1 M_{\odot} . Similarly, we indicate a limit of 2-Gyr by the right most part of the dashed line, i.e., when $G_{BP} - G_{RP} > 0.9$.

Table 2. Statistics of CHeBs in the MW dSphs

	(1)	(2)	(3)	(4)	(5)	(6)	(7)	(8)	(9)	(10)
Name	$R_{ m ell}$	(R_1, R_2)	$N_{\rm r}$	$N_{\rm net}$	S/N	$\Sigma_{ m bg}$	$N_{\mathrm{Contam.}}$	$p_{ m MW}$	N	N
	(deg; kpc)	(deg)				(deg^{-2})			$(> 1.8 {\rm M}_{\odot})$	$(> 2.04 {\rm M}_{\odot})$
Sculptor	1.1; 1.65	(1.2, 5.0)	91	90	9.4	0.47 ± 0.07	1.3 ± 0.2	5×10^{-129}	63	39
Sextans	0.8; 1.18	(1.0, 5.0)	54	48	6.53	3.4 ± 0.19	6.0 ± 0.3	1.4×10^{-32}	37	26
UMi	1.48; 1.95	(3.0, 5.0)	44	42	6.31	0.67 ± 0.10	2.1 ± 0.3	6×10^{-42}	29	22
Draco	0.5; 0.72	(0.8, 5.0)	32	31	5.43	2.37 ± 0.16	1.3 ± 0.1	4.6×10^{-33}	14	8
Carina [†]	0.4; 0.74	(0.35, 0.7)	95	85	8.63	38.7 ± 4.96	10.2 ± 1.3	2.4×10^{-57}	69	42
Fornax [†]	1.3; 3.16	(1.5, 2.5)	964	923	29.6	11.3 ± 0.8	40.8 ± 2.9	1.4×10^{-933}	687	353

Notes: Columns (1-6): Relevant parameters for the selection of CHeB candidates, see Sect. 3.3.1. Column (7): Contamination counts within the elliptical area covered by $R_{\rm ell}$, inferred from the contamination density $\Sigma_{\rm bg}$. Column (8): Probability that all CHeB candidates are due to contamination by MW stars. Columns (9-11): Counts of CHeB candidates when considering only stars with mass larger than 1.8 and 2.04 M_{\odot} , which correspond to twice the turnoff mass for a stellar population with an age of ≤ 7 and ≤ 5 Gyr, respectively. The parameters for other dSphs than Sculptor are derived from Appendix A.

[†] The methodology of Appendix A was used to derive parameters for Carina and Fornax, which distances are too large and requires a deeper photometry than that of *Gaia*.

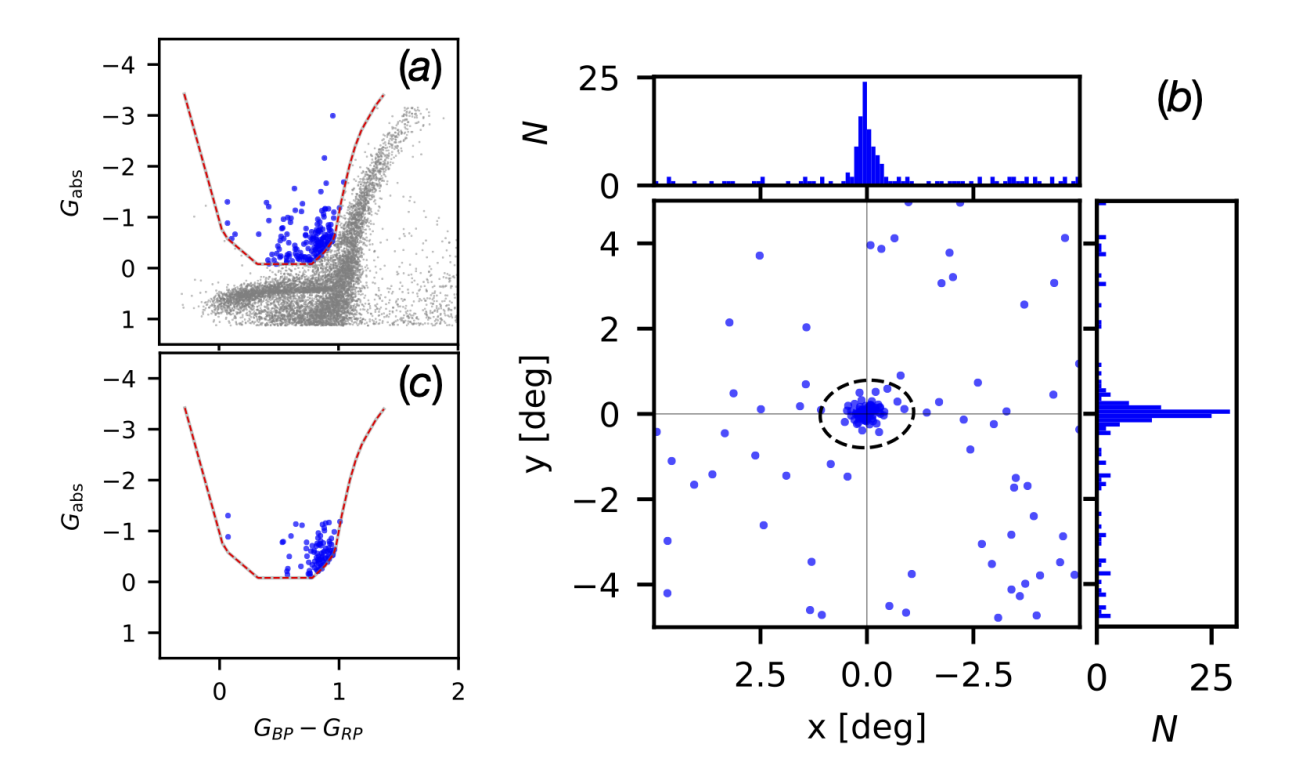


Fig. 4. Selection of CHeB candidates and their spatial distribution. Panel-(a), a rough CMD selection of CHeB candidates (blue dots) in the full field of 5×5 sq. deg. The PM-selected sample in the same field is plotted in gray dots. Panel (b), the spatial distribution of the rough CHeB candidates, with histograms of counts projection on each axis for showing the significant concentration of the CHeB candidates at the Sculptor's center. Panel (c) shows only the CHeB candidates that are selected by their locations in the CMD, spatial location within the elliptical radius of 1.1 degree. The red dashed line in both panel (a) and (c) is the CHeB selection condition (see Figure 3 and Sect. 3.3.1).

by binaries (i.e., BSSs). We discuss this possibility later (see Sect. 5), whereas here we pursue our analysis of their properties under the assumption that they are young stars.

For a more precise selection of the CHeB population, we further exclude AGB, HB (also RR-Lyrae), and MS stars. This leads to the red-dashed line delineated in Figure 3, which defines our method to select CHeB stars, that is to say that selected stars lie above the line. To exclude RR-Lyrae, we set a limit of 0.55 magnitude above the median HB around $G_{BP}-G_{RP}=0.5$. Since different galaxies have a different magnitude of the HB, the lower limits of the red-dashed line are different for each galaxy.

It is worth to note that our selection may include young stars in the SG phase, which are also of interest for the goals of our paper. The impact of considering the later stars is small because the SG phase for intermediate-mass stars is relatively short (by a factor of about 6 as shown in Figure 1, for example) when compared to the duration of the CHeB phase.

3.3.2. Step 2: Statistical significance of CHeB candidates

Figure 4 presents our selection criteria of the CHeB candidates in Sculptor. Panel (a) shows the CMD of the PM-selected sample (gray dots) within 5×5 sq deg region. We mark in blue the stars that are consistent with a CHeB phase. This is a rough selection because it picks up CHeB candidates over an extremely large sky area. The stars selected far from Sculptor may be due to contamination by MW stars. Panel (b) shows the spatial distribution of the rough selection of CHeB stars (see blue dots), which present a strong concentration in the Sculptor center, as also indicated by the peaks of the two histograms of star counts projected on each axis, respectively. Besides the concentration

in the central region, part of the candidates in the rough selection spread almost homogeneously far from Sculptor over the full field of view, as expected for MW stars. We can consider the latter to evaluate the background level of the contamination by MW stars.

We first calculated the surface density of the contamination background ($\Sigma_{\rm bg}$), by counting the number of the rough CHeB candidates within an annulus from R_1 to R_2 ; namely, 1.2 to 5.0 degree from the Sculptor center (see Table 2). We then derived the MW contamination level, which is found to be $\Sigma_{\rm bg} = 0.47 \pm 0.07~{\rm stars/deg^2}$. This low contamination density level is partly related to the location of Sculptor at high Galactic latitude of $-78.11~{\rm degree}$, far from the MW disk. It also results from the efficient filtering by proper motion, as most of MW stars have distinguishable proper motions when compared to those of Sculptor.

At this point, we should be able to evaluate the significance of the concentration of the CHeB candidates and their probability of belonging to Sculptor. We define the signal-to-noise ratio (S/N) of the net number count of CHeB candidates using a set of Eqs (1):

$$A = \pi (1 - e)R_{\text{ell}}^{2},$$

$$N_{\text{net}} = N_{\text{r}} - A\Sigma_{\text{bg}},$$

$$S/N = N_{\text{net}} / \sqrt{N_{\text{r}}},$$
(1)

where $R_{\rm ell}$ is the elliptical radius (see the dashed-line ellipse in the panel (b) of Figure 4) that describes the morphology of Sculptor together with PA and e (see Table 1), $N_{\rm r}$ gives the counts inside the elliptical area A, $N_{\rm net}$ gives the net count after subtracting the MW contamination, namely, $N_{\rm Contam.}$, which

is calculated through $N_{\rm Contam.}=A\Sigma_{\rm bg}$. We have let $R_{\rm ell}$ vary and its adopted value is given after maximizing the signal-to-noise ratio (S/N). We have detected a significant number of CHeB candidates (N_r) in Sculptor, which is far more superior than the expected contamination from the MW ($N_{\rm Contam.}$). We then calculate the probability that MW stars could be mistaken as CHeB candidates, assuming a Poisson distribution for counts. The probability of k events for a mean count of λ is given by: $p_k = \lambda^k e^{-\lambda}/k!$. For Sculptor, it leads to a count of 91 CHeB stars within $r_{\rm ell} < 1.1$ deg. The MW contamination in the same area is 1.3 ± 0.2 stars. Then the probability of 91 counts come the fluctuation of 1.3 is $p_{\rm MW} = 5 \times 10^{-129}$, which rules out the possibility of a contamination by MW stars. All the above quantities are listed in Table 2, together with those for other dSphs (see also Appendix A).

3.4. Ages, masses, and metallicities of CHeB stars in dSphs

By definition, our selection of CHeB stars is presumably made of young stars, namely, with ages smaller than 2-Gyr. Based on their locations in the CMD, we further investigated the details of their stellar parameters, such as masses, metallicities, stellar ages, and evolutionary phases for the CHeB candidates. For five out of the six galaxies studied, we only have photometric data to perform this estimate. For Sculptor, instead, we also have spectra, that allow to derive metallicities, this breaks the age-metallicity degeneracy, that is one of the sources of uncertainty. We tested two methods, one (i.e., "method tracks") based on evolutionary tracks, and no information on metallicity for individual stars beyond what can be inferred from CMD. The other one (namely "method isochrones") is based on isochrones, which we applied only to Sculptor, which makes use of the spectroscopic metallicities discussed in Sect. 4. In principle, the two methods should provide consistent results, because both methods are based on the same evolutionary track library, PARSEC. In practice, the way of building and using tracks and isochrones (e.g., parameter spacing in age, mass, and metallicities, or algorithms used to pick a solution) may cause some differences in results. The results are provided in Table 3 and the main conclusion is that whatever the details of the method used to estimate ages and masses, the ages of these stars are young and their masses large enough to classify them as intermediate mass stars. That is stars that, when on the main sequence were of spectral type A or В.

3.4.1. Ages, masses, and metallicities based on photometry and evolutionary tracks

We first prepared a sample of evolutionary tracks within the metallicity range of each dSph (see Table 1) and within a mass range of [1, 8] M_{\odot} , respectively. The mass range is wide enough to cover all CHeB candidates. We have let the stellar age of the tracks free in this calculation to avoid possible cutoff biases.

For a given star, the mass, metallicity, age, and evolution phase have been estimated through all possible evolutionary tracks that are covered by 1 sigma error in photometry. To identify the most probable evolutionary track, we defined a parameter of elapsed time that a star will spend to pass on a given track, after accounting for the window of the error bar. Therefore, the slow evolutionary track is more likely to be observed. Appendix B describes the algorithms we used for the solutions reported for individual stars. The final results for CHeB candi-

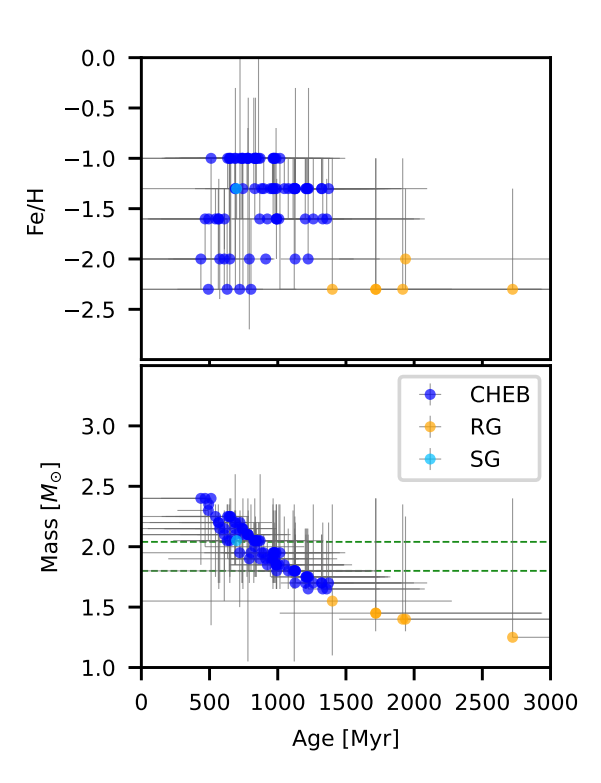


Fig. 5. Age-metallicity (left), and age-mass (right) relations for CHeB stars in their different evolutionary phases (indicated by color explained in the legend) for Sculptor. The three dashed lines in the middle panel indicate the masses of 1.8 and 2.04 M_{\odot} , respectively.

dates of Sculptor is presented in Figure 5, and Figure A.2 for other dSphs.

Ages and masses based on photometry, isochrones, and spectroscopic metallicities, in Sculptor

For the 14 stars in Sculptor discussed in Sect. 4, we can take advantage of the spectroscopic metallicities, thus breaking the agemetallicity degeneracy. To estimate ages and masses, we use the color magnitude diagram G_{BP} – G_{RP} vs. G_{abs} . We compared each star to PARSEC (Bressan et al. 2012) isochrones, within 0.3 dex of the spectroscopic metallicity, corresponding to 7 metallicity bins. The age steps were of 100 Myr. We then selected among the isochrones the same evolutionary stage. The complex topology of the isochrones, as illustrated in Fig. 1 makes this exercise ambiguous. For each star, for each age and evolutionary phase, we interpolated in the isochrone the G_{abs} corresponding to the star's $G_{BP} - G_{RP}$. Then on this curve in the CMD, we interpolated the values of age and mass corresponding to the observed $G_{\rm abs}$. For most evolutionary phases, there was no solution, since $G_{\rm abs}$ was either larger than the maximum or smaller than the minimum values on the curve. We derived two or three solutions for each star, only for star Sc119 we could find only one solution. In Table 3, we report only two solutions, corresponding to the lowest and highest possible mass. For each star we also report the corresponding evolutionary stage.

To verify the impact of distance error to the stellar parameters estimates, we repeated the above estimation procedures by considering an additional error in the magnitude of stars due to the uncertainty of distance modulus (Table 1). We found that the differences of the two estimations show an unbiased scatter of 24% in age and 8% in mass determination, respectively. These

Table 3. Age and mass estimates for the Sculptor stars observed with Giraffe.

				Me	thod tra	icks					N	Method is	sochrone	es		
	solution0			solution1			S	solution2			solution1			solution2		
Name	age	mass	phase	age	mass	phase	age	mass	phase	age	mass	phase	age	mass	phase	
	(Myr)	$({ m M}_{\odot})$		(Myr)	$({ m M}_{\odot})$		(Myr)	$({ m M}_{\odot})$		(Myr)	(M_{\odot})		(Myr)	$({ m M}_{\odot})$		
Scl2	629	2.0	CHeB	629	2.0	CHeB	473	2.4	RGB	499	2.5	CHeB	389	2.7	SG	
Scl3	494	2.4	CHeB	494	2.4	CHeB	494	2.4	CHeB	722	2.2	CHeB	331	2.8	SG	
Scl8	544	2.2	CHeB	1206	1.8	AGB	512	2.4	CHeB	731	2.2	CHeB	358	2.8	SG	
Scl9	467	2.4	CHeB	790	2.0	CHeB	467	2.4	CHeB	703	2.3	CHeB	317	2.8	SG	
Scl12	912	1.9	CHeB	912	1.9	CHeB	848	1.9	AGB	757	2.1	SG	339	2.8	SG	
Scl19	781	2.1	CHeB	4715	1.1	RGB	468	2.4	RGB	399	2.8	SG				
Sc129	436	2.4	CHeB	962	1.9	AGB	436	2.4	CHeB	795	2.0	AGB	752	2.1	CHeB	
Sc131	980	1.9	CHeB	1301	1.7	CHeB	581	2.3	CHeB	1356	1.7	CHeB	482	2.3	SG	
Scl38	1016	1.9	CHeB	1171	1.6	CHeB	537	2.4	CHeB	1393	1.7	CHeB	521	2.3	RGB	
Scl47	608	2.1	CHeB	1403	1.6	RGB	521	2.3	RGB	608	2.1	CHeB	555	2.2	RGB	
Scl61	782	2.1	CHeB	852	2.0	CHeB	613	2.2	CHeB	2168	1.4	CHeB	658	2.0	CHeB	
Scl68	655	2.2	CHeB	1062	1.8	CHeB	523	2.4	CHeB	962	1.9	CHeB	394	2.6	SG	
Sc170	723	2.2	CHeB	957	1.9	CHeB	488	2.3	CHeB	904	2.0	CHeB	364	2.6	SG	
Scl75	740	2.1	CHeB	1309	1.7	CHeB	630	2.2	CHeB	1144	1.8	CHeB	449	2.4	SG	

Two types of solutions from "method tracks" and "method isochrones" are provided. The solutions "1" and "2" correspond to the lowest and highest possible mass in different methods, respectively. The solution "0" of the "method tracks" is the most probable solution based on the elapsed-time argument.

scatters are small compared to the uncertainty due to the complexity of stellar evolution, which is usually larger than 50%-100% in age and about 20% in mass, as shown in Figure 5. We also note that the counts in columns 9 and 10 in Table 2 are marginally affected within the Poisson statistical errors when considering the error in distance, specifically, $N(>1.8~{\rm M}_{\odot})=69$ and $N(>2.04~{\rm M}_{\odot})=35$ for Sculptor. Thus, the uncertainties of 5 kpc (De Boer et al. 2012a) in the distance of Sculptor provides an uncertainty in mass and age negligible with respect the uncertainty related to the phase in which the stars are. We applied the same test to the other dSphs in Table 2 using the "method tracks" and our conclusion on the impact of distance error stands the same as for Sculptor.

4. Spectroscopic study of the CHeB population in Sculptor

4.1. GIRAFFE spectra

We cross-matched our CHeB candidates (see Sect. 3.3.1) with the ESO archive. A sample of 28 Giraffe spectra (setting LR08 for detecting the Ca II IR triplet) of CHeB star candidates was selected satisfying the CMD selection shown in Fig. 4, with the additional condition that $S/N \ge 20$ (from the ESO archive). The targets are listed in Table 4. The selected spectra belong to programs 0100.B-0337, 0101.B-0189 (P.I. E. Tosltoy), and 0101.D-0210 (P.I. A. Skúladóttir). All the spectra we retrieved from the ESO archive were previously analyzed and discussed by Tolstoy et al. (2023). Here, we provide an independent analysis and discuss the similarities and differences with Tolstoy et al. (2023). The ESO archive provides extracted spectra, correction for the earth's motion (the heliocentric correction), but the spectra are not sky-subtracted. A median sky spectrum was computed from the sky spectra accompanying each spectrum from the ESO archive and then subtracted from the object spectrum. A spectral interval around one of the Fe I lines used is shown in Fig. 6, along with the relevant synthetic spectra. The radial velocities

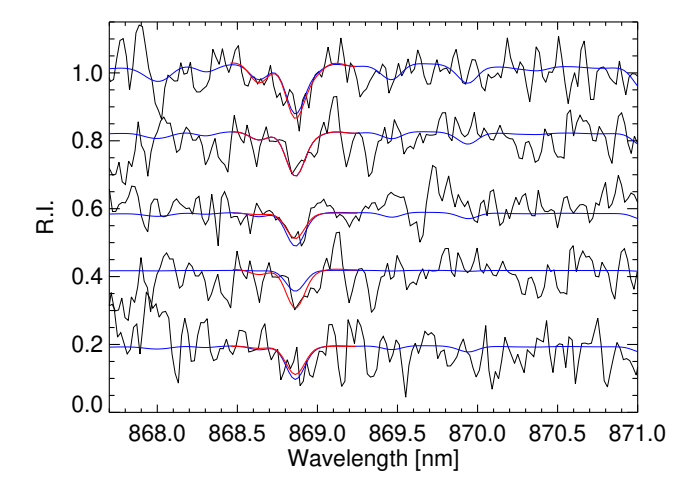


Fig. 6. Observed spectra (solid black) normalised and vertically shifted for presentation purpose, compared to synthetic spectra (solid blue) in the wavelength range of the 868.86 nm Fe I line and the best fit of the Fe feature (solid red). The spectra are ordered in decreasing metallicity, from top (the most metal-rich) to bottom (the most metal-poor): Scl 12, Scl 19, Scl 9, Scl 29, and Scl 2.

(see Sec.4.2) and abundances (see Sect. 4.3) derived from the spectra allowed us to confirm or reject the membership of the stars to the galaxy.

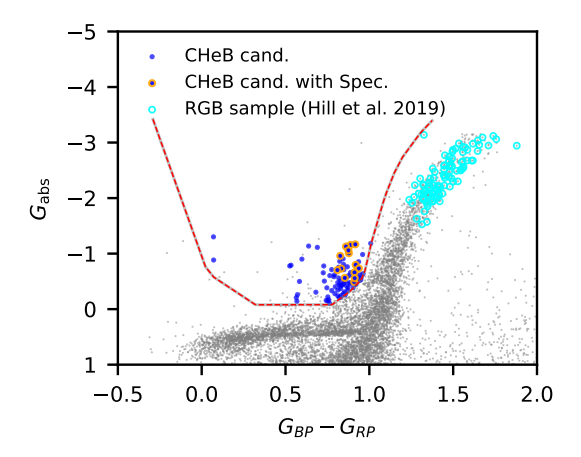
4.2. Radial velocities

For each star, we measured the radial velocity using our own code for template matching. The template consists of a synthetic stellar spectrum chosen according to our estimate for the atmospheric parameters and a telluric absorption theoretical spectrum from Bertaux et al. (2014). The stellar instrumental radial velocity and that of the telluric lines were adjusted independently, and the final radial velocity was obtained by subtracting the velocity of the telluric lines from the instrumental radial velocity.

Table 4. Radial velocities of the analyzed stars

Target	RA	Dec	$v_{\rm rad}$
	(deg J2000)	(deg J2000)	$(km s^{-1})$
Scl0	15.549990	-33.718388	78 ± 4
Scl1	14.995166	-33.714305	118 ± 6
Scl2	15.525830	-33.662277	104 ± 1
Scl3	15.302080	-33.758472	110 ± 1
Scl5	15.404990	-33.783555	104 ± 7
Scl8	15.055830	-33.754583	106 ± 6
Scl9	14.939249	-33.688861	130 ± 1
Scl12	15.696240	-33.778249	93 ± 3
Scl16	15.140749	-33.775027	106 ± 1
Scl18	15.159208	-33.808833	104 ± 2
Scl19	15.219833	-33.690944	112 ± 4
Scl21	15.458740	-33.845388	127 ± 3
Scl21a	15.458740	-33.845388	102 ± 2
Scl23	15.181958	-33.717388	112 ± 1
Scl24	14.831166	-33.627361	121 ± 1
Scl27	14.893208	-33.511333	112 ± 1
Scl29	15.138708	-33.620277	112 ± 1
Scl31	15.158166	-33.622749	109 ± 1
Scl38	15.372083	-33.851805	124 ± 3
Scl40	15.268166	-33.688972	111 ± 1
Scl47	14.770208	-33.631972	112 ± 1
Scl50	14.943333	-33.960083	146 ± 1
Scl59	14.745166	-33.940749	108 ± 1
Scl61	15.466249	-33.648722	83 ± 1
Scl68	14.637208	-33.710361	99 ± 1
Scl69	14.648083	-33.556722	103 ± 3
Scl70	14.699624	-33.495861	117 ± 3
Scl75	15.152041	-34.101361	121 ± 1

The measured radial velocities are given in Table 4. For one star in Table 4, we have two spectra (Scl21 and Scl21a) from program 0101.B-0189 and these were treated independently. There is a difference of $25.5 \,\mathrm{km \, s^{-1}}$ between the two measurements. The two spectra were observed at different epochs, separated by approximately one year. The simplest explanation is that the star Sc121 is a binary; thus, we excluded it from the chemical analysis. Battaglia et al. (2008) measured a mean radial velocity of 110.6 km s⁻¹ with a dispersion of 10.1 km s⁻¹ for Sculptor, on the basis of 470 stars having Giraffe spectra. We considered all stars having a radial velocity that lies within three times the velocity dispersion from the mean radial velocity of Battaglia et al. (2008) as Sculptor members. This criterium excludes targets Scl0 and Scl50, leaving us with 25 radial velocity members in the sample, and then 24 after removing Scl21. The mean radial velocity of our retained 24 stars is 109.6 km s⁻¹ with a standard deviation of 9.8 km s⁻¹ in excellent agreement with the value of 10.1 km s⁻¹ derived by Battaglia et al. (2008). The spectra we analyzed were also previously studied by Tolstoy et al. (2023). For the 24 member stars in our sample (which were also considered as Sculptor members in that study), their mean radial velocity is $109.6 \, \text{km} \, \text{s}^{-1}$ with a standard deviation of $9.1 \, \text{km} \, \text{s}^{-1}$; this is in excellent agreement with our result. The average difference, in the sense our radial velocities minus Tolstoy et al. (2023), is $-0.02 \,\mathrm{km}\,\mathrm{s}^{-1}$ with a dispersion of 5.9 km s⁻¹. Using 3- σ criteria, we excluded 2 out of the 27 stars (including a binary) listed in Table 4 from membership. This suggests that the PM-selected sample is effective, with 25 out of 27 stars identified as potential members, even though the size of this verification sample is statistically limited.



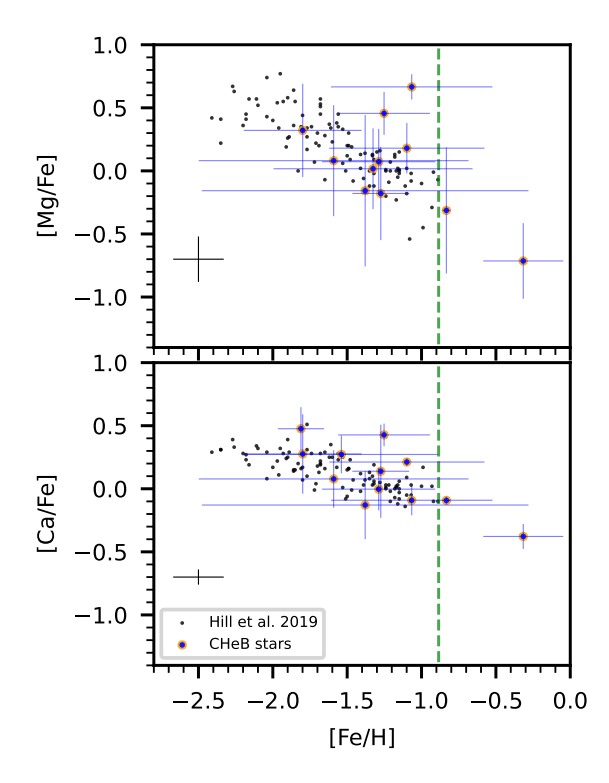


Fig. 7. CMD of Sculptor showing different samples (top). Blue dots for the CHeB candidates; blue dots with orange circle for the CHeB candidates with Giraffe spectra with $S/N \ge 20$; open cyan circles for the RGB sample from Hill et al. (2019). The gray dots and the red dashed line have the same meanings as in Figure 4. Middle and bottom panels give a comparison of the measured metallicities for the CHeB candidates with those of RGB stars measured by Hill et al. (2019, small black dots). The typical error bars of different elements for the RGB stars are plotted in black on the lower-left of each panel, respectively. In these panels, the green dashed line indicates the upper limit of [Fe/H] for the RGB sample.

4.3. Atmospheric parameters and abundances

The atmospheric parameters were derived from the *Gaia* photometry, as described in Lombardo et al. (2021), namely, assuming an E(B-V) and a distance in Table 1 for Sculptor. For each star, we assumed the highest mass listed in Table 3, which impacts the derived surface gravity and thus the Ca II abundances. The micro-turbulent velocity was derived from the calibration of Mashonkina et al. (2017). We then ran MyGIsFOS (Sbordone et al. 2014) to derive the abundances of Fe, Mg, and Ca of CHeB

Table 5. Atmospheric parameters and chemical abundances of the stars in this study.

Target	$T_{ m eff}$	$\log g$	$v_{ m vturb}$	[Fe/H]	σ(FeI)	N(FeI)	[Mg/H]	[Mg/Fe]	σ(MgI)	N(MgI)	[Ca/H]	[Ca/Fe]	σ(CaII)	N(CaII)
8	(K)	80	$(km s^{-1})$	[/]	- ()	()	[8/]	[-:-8/3]	* (8-)	- (- : - 6 -)	[1,]	[4]	- ()	(- 11)
Scl2	5354	2.56	1.66	-1.539	0.650	1				0	-1.267	0.272	0.050	1
Sc13	5511	2.45	1.77	-1.066	0.543	2	-0.400	0.666	0.100	1	-1.157	-0.091	0.040	1
Scl8	5380	2.54	1.64	-0.833	0.027	3	-1.146	-0.313	0.500	1	-0.925	-0.092	0.050	1
Scl9	5429	2.42	1.75	-1.099	0.522	3	-0.919	0.180	0.200	1	-0.886	0.212	0.010	2
Scl12	5551	2.50	1.71	-0.316	0.269	3	-1.031	-0.714	0.300	1	-0.694	-0.378	0.033	1
Scl19	5355	2.61	1.63	-1.092	0.753	2				0				0
Sc129	5327	2.24	1.82	-1.326	0.669	2	-1.308	0.017	0.320	1				0
Scl31	5621	2.56	1.84	-1.811	0.155	2				0	-1.336	0.476	0.057	2
Sc138	5368	2.56	1.65	-1.252	0.309	2	-0.796	0.456	0.170	1	-0.826	0.427	0.030	1
Scl47	5258	2.38	1.74	-1.799	0.396	4	-1.478	0.321	0.370	1	-1.522	0.276	0.105	2
Scl61	5499	2.53	1.77	-1.591	0.907	2	-1.510	0.081	0.440	1	-1.514	0.078	0.076	3
Scl68	5594	2.52	1.80	-1.274	0.191	2	-1.453	-0.179	0.370	1	-1.134	0.139	0.123	2
Sc170	5444	2.45	1.76	-1.288	0.381	3	-1.215	0.073	0.260	1	-1.291	-0.003	0.056	2
Sc175	5574	2.56	1.77	-1.379	1.098	2	-1.536	-0.157	0.600	1	-1.508	-0.129	0.090	1

Notes: N(FeI), N(MgI), and N(CaII) are the numbers of FeI, MgI, and CaII lines, respectively, in the spectra of each star.

candidate stars. We were finally left with 14 stars, for which the spectra have sufficient S/N values to provide an acceptable accuracy for their abundances. The atmospheric parameters and abundances are given in Table 5.

In Fig. 7, we compare our abundances with those of RGB stars from Hill et al. (2019). By and large, our measurements are compatible with those of Hill et al. (2019). Our errors are considerably larger, in the first place because our targets are 3 to 1.5 magnitudes fainter than those of Hill et al. (2019); in the second place, we have a lower resolution and a smaller spectral coverage. Two facts are worth noting: our sample extends to higher metallicities with respect to that of Hill et al. (2019) and it also lacks the most metal-poor stars that are present in the Hill et al. (2019) sample. The comparison with the analysis of Tolstoy et al. (2023) is less straightforward. While we measured three elements from these spectra, Tolstoy et al. (2023) measured the equivalent widths of the Ca II 854.2 nm and 866.2 nm lines and used the calibration of Starkenburg et al. (2010, Equation (5)) to derive the metallicities. A direct comparison of our [Fe/H] values with those of Tolstoy et al. (2023) shows a large discrepancy, with our values being systematically more metal-rich, up to +1.4 dex. However, one has to keep in mind that the Starkenburg et al. (2010) calibration has been derived and is valid only for RGB stars as duly noted by Tolstoy et al. (2023), who underline that their metallicities are valid only for RGB stars. In fact the effective temperature of the star is implicitly taken into account through its V magnitude⁵. An inspection of Fig. 7 (top panel) shows that while there is a clear relation between magnitude and color (and, therefore, $T_{\rm eff}$), along the RGB, this does not exist among CHeB stars, which occupy a narrow range in color, but span almost one magnitude in G_{abs} , with no clear correlation between the two. We therefore conclude that the discrepancy between our [Fe/H] values and those of Tolstoy et al. (2023) is mainly due to the the fact that the Starkenburg et al. (2010) calibration is not applicable to CHeB stars.

5. Discussion

In this paper, using theoretical evolutionary tracks, we have been able to estimate masses and ages for stars that occupy the region

expected for young stars in the CHeB phase. In this way, for Sculptor, we have identified a population of 91 young and massive stars with ages from 250 to 1500 Myr old, with masses of $\geq 1.6 \text{ M}_{\odot}$; this includes 63 (69%) and 39 (43%) stars that are more massive than 1.8 and $2.04\,M_{\odot}$, respectively (see the last columns of Table 2). Although some could also be in the SG phase; if so, that indicates they are even younger and more massive than if they were in the CHeB phase. In principle, our selection of CHeB may include the Type II Cepheids which are old (~ 10 Gyr) and low-mass stars of about 0.5–0.6 M_{\odot} (Bono et al. 2020). By comparing to the Gaia Cepheid catalogs (Clementini et al. 2023; Ripepi et al. 2019)⁶, we found none of our CHeB candidates to be a type II Cepheid. This suggests that the occurrence of type II Cepheids is very rare in the MW dSphs, which is consistent with former studies (see Monelli & Fiorentino 2022). We need to verify whether alternative explanations, other than recent star formation, may be consistent with the observations. In the following we examine two possibilities: either CHeB candidates are "rejuvenated" stars (i.e., evolved BSSs) or they are truly young and have originated in the turbulent star formation events associated to ram pressure caused by a recent entry of dwarfs into the MW halo (see Papers I, II, and III).

5.1. Interpretation of CHeB candidates in dSphs as evolved BSSs

We want to discuss the possibility of interpreting the CHeB stars as evolved BSSs. This requires a possible connection between these stars and the stars that appear in the blue plume and on the upper main sequence. We discuss these two regions of the CMD separately.

5.1.1. Connection with the blue plume

Momany et al. (2007) carried out an extensive study of blue plumes in Local Group dSphs, excluding Fornax, known to possess a young population. They established an anticorrelation between the fraction of BSSs and the luminosity of the galaxy. They concluded that this anti-correlation could be used to discriminate blue plumes made up mainly by BSSs, which follow

 $^{^{5}}$ In fact, through the difference between its V magnitude and that of the Horizontal Branch.

⁶ This includes a direct cross-matching with the Cepheid table in DR3, namely vari_cepheid.

this anti-correlation, and blue plumes that contain a significant young population, such as Carina, that do not follow this anti-correlation. They never excluded the presence of a small fraction of young stars, even in blue plumes dominated by BSSs stars. A similar study was performed by Santana et al. (2013), with different data and techniques. They found that the fraction of BSSs is either independent of the galaxy luminosity, or there is a mild anticorrelation, similar to that found by Momany et al. (2007). They also concluded that the blue plumes in the galaxies studied by them could comprise also a small fraction (1%–7%) of young (age of the order of 2.5 Gyr) stars.

The blue plume stars in Sculptor and Fornax have been studied in detail by Mapelli et al. (2009). Based on considerations on the radial distribution of BSSs stars and on dynamical simulations with the code of Sigurdsson & Phinney (1995), they conclude that while in Fornax the "blue plume" comprises a mixture of young stars and BSSs, the "blue plume" of Sculptor can be well explained as being made exclusively by BSSs. However, in their appendix A1, Mapelli et al. (2009) also point out that the interpretation of the "blue plume" as composed by stars of age 2-3 Gyr cannot be ruled out.

De Boer et al. (2012a, see their Fig. 8) found that 95.5% (84%) of Sculptor dSph stars are older than 8 Gyr (10 Gyr), respectively. All these stars are metal poor (Fe/H < -1.5). This is supported by Bettinelli et al. (2019) who found the whole stellar population in Sculptor to be older than 11 Gyr. For an old (≥ 10 Gyr), and metal poor stellar population, a turnoff star has a mass smaller than 0.8 M_{\odot} (see Figure 8). If we account for the ~ 11.5% of stellar ages between 8 and 10 Gyr, the turnoff mass limit goes to $0.9~M_{\odot}$. We consider these two values as the real limits for producing BSS from binary stars, since to reach 1 M_{\odot} for the turnoff mass needs to consider the less than 1% stars having an age of 5 Gyr old according to the SFH from De Boer et al. (2012a). A higher mass than the turnoff would imply that the star has already completed its evolution and would have already evolved to the white dwarf stage. If a BSS is formed through mass accretion in a binary system or from a fusion of two stars it should not have a mass larger than twice that of a turnoff star; namely, less than 1.6, and (for a small fraction) 1.8 M_{\odot} . In Figure 1, we show an evolutionary track of a simulated BSS formed by the fusion of two 0.8 $\ensuremath{M_{\odot}}$ stars, resulting in a star of 1.57 M_{\odot} . However, Table 2 shows that the majority (63 among 91, i.e., 69%) of CHeB candidates possess masses well above 1.8 M_{\odot} , whichever the way we estimate the mass. Blue stragglers that have masses larger than twice the mass of turnoff stars are known both in open clusters (e.g., M 67, Milone et al. 1992) and globular clusters (e.g., NGC 6397, Saffer et al. 2002). In Appendix C, we estimate how efficiently a fusion of a triple system can form massive BSSs. We have concluded that this extreme mechanism is unlikely able to explain our massive CHeB population.

If we consider our spectroscopic analysis of Sculptor stars, Fig. 7 shows that the CHeB candidates are relatively more metal rich, on average, with a lack of stars at the low metallicity end and a few stars showing higher metallicity with respect to the RGB sample of Hill et al. (2019). This does not favour a BSS origin for most CHeB candidates, for which one would have expected a similar distribution of metallicity than for the RGB general population from which they should come. To summarize, the four difficulties with interpreting CHeB candidates as BSSs in Sculptor dSph are as follow.

1. It is not possible for a BSS to form with a mass of $\geq 1.8\,M_\odot$ from an old population of stars with masses $\leq 0.8-0.9M_\odot$

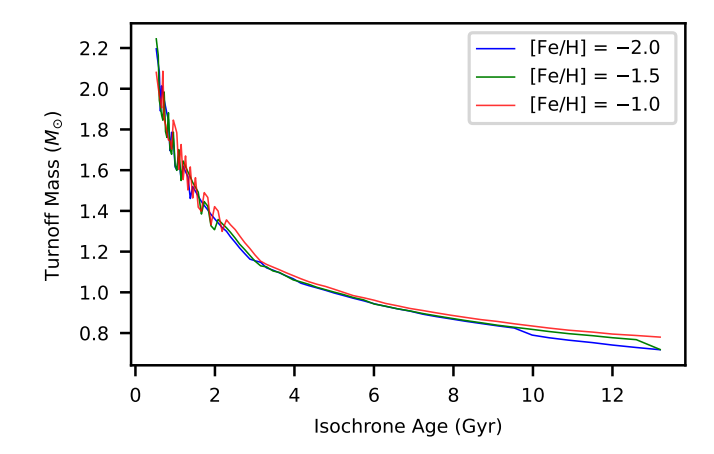


Fig. 8. Turnoff mass of isochrones of different metallicities and ages.

without involving at least three such stars. It appears unlikely that all these stars were formed in triple or higher multiplicity systems.

- 2. We found 39 CHeB stars with mass larger than 2.04 M_{\odot} (see the last column of Table 2), while none of them can be predicted from the turnoff mass even if their progenitors had, in fact, come from the rare (<1%) population of 5 Gyr old stars (turnoff mass of 1 M_{\odot} , see Figure 8), according to the SFH from De Boer et al. (2012a).
- 3. The lack of evolved blue stragglers with [Fe/H] < -2.0.
- 4. Two stars (out of 14, i.e., 14%) more metal-rich than the most metal-rich stars observed on the RGB.

5.1.2. The upper main sequence in Fornax and Sculptor

When comparing the synthetic CMD (see Sect. 5.2 for details) to Sculptor's CMD (i.e., the panels (b) to (c) of Figure 9), we may notice there are numerous upper main sequence (UMS) stars predicted by the theory, while there are only a few in Sculptor. We established our statistics by defining a UMS selection on the CMD and comparing the counts to that of CHeB. According to the result in Table 6, the observation shows a lack of UMS stars by at least factor of 3. This could be an indication that the CHeB candidates are not young stars. As reference, we examined the situation in Fornax and Carina, which are known to have experienced star formation in the recent 2 Gyr; with particularly young stars of 150-Myr old identified in Fornax (De Boer et al. 2012b; Saviane et al. 2000; Stetson et al. 1998). Regions of selection and statistical results are shown in Figure 9 and Table 6, respectively. Surprisingly, we found that Fornax and Carina show the same lack of UMS stars as in Sculptor.

We have tried to vary SHF and simulate synthetic CMD (as described in Sect. 5.2) in order to solve the discrepancy of lacking of UMS. However, we found this is impossible because to explain the distribution of high mass CHeB stars (i.e., $> 2.04~M_{\odot}$), we would need stars younger than ≈ 700 Myr (see Figure 5 and Figure A.2) and the synthetic CMDs below this age always predict more UMSs than CHeBs.

To reconcile the observations in Fornax with theory, we may envisage to assume a non-standard initial mass-function (IMF) that is truncated at the low mass end, at about 1.8 M_{\odot} . If there were any star formation taking place during the infall in a dSph, its gas may be strongly affected by the perturbation introduced by ram pressure. A recent work by Hennebelle et al. (2024) suggests that star formation could be inefficient towards the low

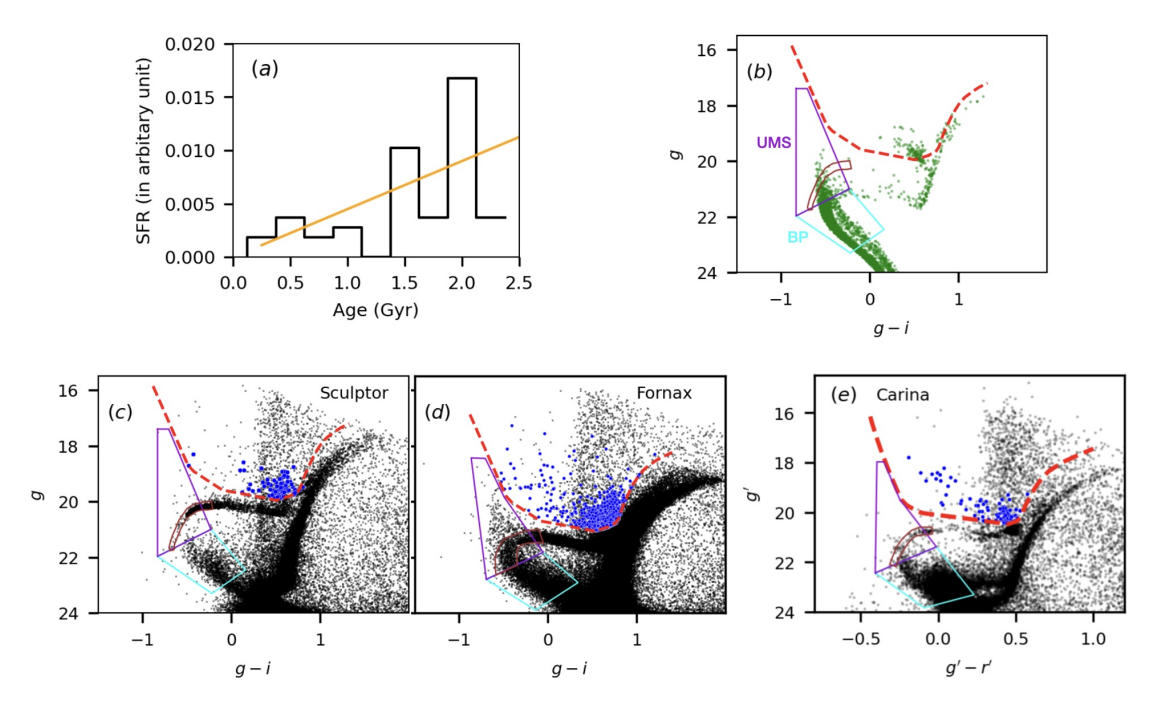


Fig. 9. Stellar populations in simulations and dSphs. Panel (a): Recent SFH of Sculptor predicted by simulations made in Paper III (black lines), while the orange line is a linear fit to the SFH. Based on the latter fitted SFH, we simulated a synthetic CMD shown as the green points in panel (b). This synthetic CMD will be compared with Sculptor's CMD (within $r_{\rm ell} = 1.1$ deg) from the Dark Energy Survey (DES) in Panels (c), with its CHeB candidates (blue dots) superposed. In both panels, we define some regions for statistics: the red-dashed line for our CHeB selection condition; cyan polygons for the blue plume(BP) region; violet polygons for the upper main sequence (UMS) region; brown polygons for HB region that to be exclude when counting inside UMS. Panels (d) and (e) show the same content as in panel (c) but for Fornax and Carina, respectively, and the polygons are revised accordingly.

mass range in high Mach number environments, in other words, strongly perturbed gas. This theoretical prediction may explain the lack of UMS stars in Fornax, Sculptor and other dSphs.

In this work, we have demonstrated that there are consistent stellar populations in Fornax, Carina, and Sculptor. Specifically, they all exhibit very similar number ratios of CHeB-to-UMS stars. Given the fact that Fornax has been forming stars very recently, the possibility of a recent star formation in Sculptor cannot be ruled out. Sculptor is almost ten times less massive than Fornax (Hammer et al. 2019), as also supported by the UMS counts in Table 6. This may explain why the UMS stars in Sculptor cannot be recognized visually.

5.2. CHeB candidates as indicators of a recent star formation

If the CHeB candidates in Sculptor are genuine young stars due to a recent star formation, we should expect to detect the imprint of their MS counterparts in the BP to be consistent with a normal recent star formation. This could be indicated by the ratio of stellar counts between the CHeB population and the BP population. In particular, the number of CHeB stars found for Sculptor should predict more than a thousand stars in the BP. To make this consistency check, we may compare the observations to a synthetic CMD, after assuming a recent SFH.

In Paper III, we carried out a simulation dedicated to simulate the infall of Sculptor that also predicts the star formation induced by ram pressure during a recent infall. Figure 9a shows the corresponding predicted SFH from paper III (see the black histogram). The SFH can be approximated by a linear and declining star formation activity in the last 2.5 Gyr (i.e., the orange line in Figure 9a) hereafter denoted as the "predicted" SFH.

We used BaSTI to simulate a synthetic CMD of a recent star formation by assuming the predicted SFH between 0.5 to 2.5 Gyr, a Kroupa IMF (Kroupa 2001), and an averaged [Fe/H] = -1.5. The simulated synthetic CMD is shown in Figure 9 b. For improved visualization, we re-scaled the synthetic CMD to have CHeB counts of 93 (i.e., all points above red-dashed line in the figure), which is similar to that of Sculptor from *Gaia* dataset.

To make this comparison possible, we had to extend our dataset for the faint MS stars by using the deep photometry from the Dark Energy Survey (DES). We obtained stars within 1.1 degree elliptical radius centered on Sculptor from the DES data release 2 (DR2). The star-galaxy separation was done using the parameter extended_class_coadd = [0,1] for stellar sources, following the official document. We may define a BP region using a polygon (in cyan color) on the CMD (Figure 9), after avoiding the possible contamination from HB stars in the bright end and possible confusion due to photometric errors in the faint end.

Then, we go on to count the number of CHeB and BP stars, in both observed and synthetic CMD, and the values are listed in Table 6. As we have demonstrated, the Gaia detection of CHeB stars has few contamination, so we may directly compare it to the CHeB counts from the simulated CMD. For the BP population observed by DES, the MW contamination is likely very small after examining the CMD; thus, we did not apply any correction to these BP counts (listed in Table 6). The result shows that the number ratios are similar, indicating that the CHeB population detected in Gaia data is compatible with recent star formation within the last 2.5 Gyr after assuming the predicted SFH from simulation of a recent infall of Sculptor. Table 6 shows that the ratio obtained from observations is slightly larger than that from the simulated CMD. Such a difference could be due to the input IMF or possibly related to the incompleteness in the observation of DES in the magnitude range of our BP selection. The latter

Table 6. Statistics of CHeB, BP, and UMS populations.

	N_{CHeB}	N_{BP}	$\frac{N_{\mathrm{CHeB}}}{N_{\mathrm{BP}}}$	$N_{ m UMS}$	$\frac{N_{\mathrm{CheB}}}{N_{\mathrm{UMS}}}$
Synthetic CMD	116	2010	0.057	240	0.48
Sculptor	90	1169	0.077	55	1.64
Sextans	38	543	0.069	_	_
UMi	54	795	0.067	_	_
Draco	36	589	0.061	_	_
Carina	95	8065	0.012	77	1.23
Fornax	964	4794	0.201	516	1.87

Notes: N_{CHeB} is equal to N_{net} that is quoted in Table 2 for dSphs.

is especially relevant when considering that our statistics from observations also include the crowded stellar field in the center of Sculptor.

We extended this statistical test to the other dSphs, namely, Sextans, UMi, Draco, Carina, and Fornax, with the results listed in Table 6. We adopted the deep photometry of these three objects from the observations by Muñoz et al. (2018). The latter were carried out with MegaCam system, which is a different photometric system from DES; thus, we have carefully defined a BP region, which is equivalent to the BP definition in Figure 9, on the CMD in MegaCam filter system (see Appendix A for the definition of these photometric systems).

5.3. Recent star formation in dSphs during their recent infall into the MW halo

Figure 5 indicates a recent star formation from ~ 0.4 to 2 Gyr after accounting for the young stars detected in Sculptor. This is almost consistent with a single star formation burst that occurred about 1 Gyr ago. A short starburst does not necessarily result in a narrow range of metallicity, as demonstrated by the case of Boo I, for which a single starburst with a duration of only 50 Myr produced a spread in metallicities of about 2 dex (see Rossi et al. 2021, Figures 3 and 4). In spite of the large errors associated to our chemical abundance measurements in Sculptor, the spread in metallicity seems to be real. Although we cannot formally exclude the possibility that the stars share a single metallicity ([Fe/H]= -1.2 ± 0.33), this would not explain the [Mg/Fe] and [Ca/Fe] trends shown in Figure 7. The typical timescale for SN Ia enrichment depends on the star formation rate and on the IMF. Matteucci & Recchi (2001) estimated that for a single starburst, this can be as short a timescale as 40–50 Myr. The fact that the young population displays a trend in [Mg/Fe] and [Ca/Fe] implies that this timescale has been very short indeed. Zhu et al. (2024) conducted dedicated simulation to investigate the SF processes in gas-rich dwarf galaxies under conditions of ram pressure striping (RPS). Their results suggest that bursty SF appears to be a typical feature during all their simulation time until gas is completely removed from galaxies. Such bursty SF has also been observed in Fornax by Rusakov et al. (2021), and seems to be consistent with the SF induced by RPS (e.g., see the discussion in Yang et al. 2022).

If the spread in Figure 7 were due to measurement errors alone, we would not expect to see any trend among the abundance ratios. This is especially true for [Fe/H] and [Ca/Fe], for which a Kendall's τ statistics gives a 99.999% probability that they are anti-correlated. It is difficult to dismiss these findings, and they need to be explained if they result from a recent star for-

mation hypothesis. CHeB candidates of different metallicity do not show a defined age-metallicity relation (see the **top** panels of Figure 5). The ages and metallicities for the CHeB candidates in Sculptor, whether we take [Fe/H] or [Ca/H], are not correlated; however, they are expected to be undergoing a star formation event. The past history of the dSph hosts of CHeB candidate stars, as described in Papers I, II, and III, provides a plausible interpretation of the observations.

MW dSph progenitors are gas-rich galaxies, namely, dwarf irregular galaxies (dIrrs) that have recently (< 3 Gyr ago) been accreted by the MW (see Paper I). During their infall, they lost their gas due to the ram pressure of the MW halo corona. This fully transformed them from gas-rich dwarfs at equilibrium to gas-free dwarfs sufficiently out of equilibrium to explain their large velocity dispersions (see Papers II and III). The simulations carried out in Paper III showed that before being removed, the gas is affected by considerable turbulence through shocks and compression⁷. The latter phenomenon led to star formation, while the former ensures that the whole gas medium has been literally shaken, providing star formation within a mixture of gasrich clouds with various metallicities. This is consistent with the absence of a defined age-metallicity relation in Figure 5, as well as with the observed metallicity spread. This may also explain the different metallicity distributions between the old population (age > 6 Gyr) and the young population (age < 2.5 Gyr), the latter lacking the most metal-poor tail and extending to slightly higher metallicities. The fact that there is a wide metallicity overlap between the two populations implies that the gas that fuelled the starburst was not chemically homogeneous.

The role of ram pressure is twofold: i) removing the gas in infalling dIrrs and ii) mixing and compressing gas from outer region (metal poor) towards inter region (metal rich) in the galaxy. If the gas is compressed to a high enough density, there will be star formation processes ignited. Our finding that part of the CHeB candidates in dSphs are possibly young stars is consistent with the orbital history of dSphs that are revealed by Gaia proper motions. Our results support a very recent star formation associated to the recent infall of dSph progenitors (see Figure 9-a). Simulations from Paper III have successfully reproduced the observed properties for Sculptor assuming a recent infall. They predicted a very small fraction (« 1% of the total stellar mass) of stars formed in the last 1.5 Gyr during the infall of the simulated dwarf galaxy. Taking the estimated mass of the CHeB candidates, we may infer the total mass formed in Sculptor after assuming an initial mass function (IMF). Given the 91 CHeB candidates with masses ranging from 1.8 to 3.0 M_{\odot} , by inverting the Kroupa IMF (Kroupa 2001), for example, we can derive the corresponding stellar mass formed during the same time interval; this is 7200 M_o, at a star formation rate (SFR) of 3.6×10^{-6} M_{\odot}/yr over 2.5 Gyr. If we adopt a total stellar mass of $5.1 \times 10^6 \text{ M}_{\odot}$ for Sculptor (see Paper II), the mass fraction of young stars is 0.15%.

6. Conclusions

In this work, we have identified a population of apparently young, intermediate mass CHeB stars, which has been distinguished from MW foreground stars using *Gaia* DR3 PMs. They are found in several dSphs, including Sculptor, UMi,

⁷ A video realized during the Paper III modeling of a recent infall of the Sculptor dSph progenitor is available at: https://www.youtube.com/watch?v=SwxSdmfQis4

and Sextans, which were previously thought to possess only old stars, as well as Draco. For the latter, the existence of a young population was claimed by Aparicio et al. (2001), but confuted by Mapelli et al. (2007). Their ages and masses have been computed using a grid of evolutionary tracks and they have been confirmed using isochrones, for a sub-sample with spectroscopic metallicities.

Two possible channels have been considered to explain the observations of CHeB candidates. It could be that they are evolved BSSs or, alternatively, they could have been formed during the star formation induced by ram pressure at a recent epoch; namely, when gas-rich dSph progenitors entered in the MW halo and its corona.

The former hypothesis faces serious difficulties, because the stars had to have gone through very rare events of coalescence of at least three stars to form a single BSS. This conclusion is very robust since many CHeB candidates have masses in excess of $1.8\,M_\odot$, while dSph turnoff mass stars have to be smaller then $0.9\,M_\odot$. This is because 95.5% of Sculptor stars are older than 8 Gyr, leading to masses smaller than $0.9\,M_\odot$, which only allows BSS masses of less than $1.8\,M_\odot$ (much smaller than what we have observed). Furthermore, the BSS hypothesis is not sufficient to explain why some CHeB candidates have larger metallicities than RGB stars, as well as why none of them share the lowest metallicities of RGB stars.

All the CHeB star candidates are then considerably younger than the sample of Hill et al. (2019) (< 1 Gyr compared to 6 Gyr, the youngest ages in the RGB sample). Such recent star formation events are consistent with a recent infall of dSph progenitors that are expected to be gas-rich dIrrs (see paper I). During their infall, the gas was very turbulent and its whole content permanently shaken before being removed by the ram pressure exerted by the Galactic corona (see Paper III). Such a hypothesis is also supported by the comparison of number counts of CHeB stars with those UMS stars in Sculptor and Fornax. The existence of a young stellar population in Fornax has been robustly established. This peculiar series of processes explains the large velocity dispersions of dSphs (see Papers II and III). This approach is also consistent with the chemical analysis presented here; specifically, the absence of an age-metallicity relation and the spread in metallicity despite of the short-duration of these star formation events. If confirmed by further observations, this population of young-and-intermediate mass stars may be the last witnesses of very recent star formation events in dSphs, including in those reputed to possess only a very old star population.

Acknowledgements. We thank Dr. Santi Cassisi for the insightful discussions, his help in using the BaSTI and simulating the synthetic CMD. We thank Eva Grebel for her explanations of many former CMD studies of Sculptor. We are grateful to Dr. Yang Chen for his help on the use of the PARSEC stellar evolutionary tracks and the YBC database of stellar bolometric corrections. We thank Dr. Monique Spite, Dr. Marcel S. Pawlowski, Dr. Haifeng Wang, Mr. Yongjun Jiao and Dr. Hefan Li for their helpful discussions. We are also grateful to Prof. E. Tolstoy and Prof. A. Skúladóttir for their very useful comments on our paper. We are also grateful to Prof. A. Sills for providing us with the evolutionary tracks of BSS. We are grateful for the support of the International Research Program Tianguan, which is an agreement between the CNRS in France, NAOC, IHEP, and the Yunnan Univ. in China. This work presents results from the European Space Agency (ESA) space mission Gaia. Gaia data are being processed by the Gaia Data Processing and Analysis Consortium (DPAC). Funding for the DPAC is provided by national institutions, in particular the institutions participating in the Gaia MultiLateral Agreement (MLA). The Gaia mission website is https://www.cosmos.esa.int/gaia. PB and EC gratefully acnkowledge support from the European Research Council through Advanced Grant 835087 - "SPI-AKID" and from the French National Research Agency (ANR) through project

"Pristine" (ANR-18- CE31-0017). This project used public archival data from the Dark Energy Survey (DES). Funding for the DES Projects has been provided by the U.S. Department of Energy, the U.S. National Science Foundation, the Ministry of Science and Education of Spain, the Science and Technology FacilitiesCouncil of the United Kingdom, the Higher Education Funding Council for England, the National Center for Supercomputing Applications at the University of Illinois at Urbana-Champaign, the Kavli Institute of Cosmological Physics at the University of Chicago, the Center for Cosmology and Astro-Particle Physics at the Ohio State University, the Mitchell Institute for Fundamental Physics and Astronomy at Texas A&M University, Financiadora de Estudos e Projetos, Fundação Carlos Chagas Filho de Amparo à Pesquisa do Estado do Rio de Janeiro, Conselho Nacional de Desenvolvimento Científico e Tecnológico and the Ministério da Ciência, Tecnologia e Inovação, the Deutsche Forschungsgemeinschaft, and the Collaborating Institutions in the Dark Energy Survey. The Collaborating Institutions are Argonne National Laboratory, the University of California at Santa Cruz, the University of Cambridge, Centro de Investigaciones Energéticas, Medioambientales y Tecnológicas-Madrid, the University of Chicago, University College London, the DES-Brazil Consortium, the University of Edinburgh, the Eidgenössische Technische Hochschule (ETH) Zürich, Fermi National Accelerator Laboratory, the University of Illinois at Urbana-Champaign, the Institut de Ciències de l'Espai (IEEC/CSIC), the Institut de Física d'Altes Energies, Lawrence Berkeley National Laboratory, the Ludwig-Maximilians Universität München and the associated Excellence Cluster Universe, the University of Michigan, the National Optical Astronomy Observatory, the University of Nottingham, The Ohio State University, the OzDES Membership Consortium, the University of Pennsylvania, the University of Portsmouth, SLAC National Accelerator Laboratory, Stanford University, the University of Sussex, and Texas A&M University. Based in part on observations at Cerro Tololo Inter-American Observatory, National Optical Astronomy Observatory, which is operated by the Association of Universities for Research in Astronomy (AURA) under a cooperative agreement with the National Science Foundation.

Data Availability

The catalogs of the PM-selected and CheB candidates are available upon request.

References

Fernie J. D., 1990, ApJ, 354, 295

```
Aguilar L., Hut P., Ostriker J. P., 1988, ApJ, 335, 720
Aparicio A., Carrera R., Martínez-Delgado D., 2001, AJ, 122, 2524
Arenou F., 2011, in Docobo J. A., Tamazian V. S., Balega Y. Y., eds, American
   Institute of Physics Conference Series Vol. 1346, International Workshop on
   Double and Multiple Stars: Dynamics, Physics, and Instrumentation. pp 107-
   121, doi:10.1063/1.3597593
Battaglia G., Helmi A., Tolstoy E., Irwin M., Hill V., Jablonka P., 2008, ApJ,
Battaglia G., Taibi S., Thomas G. F., Fritz T. K., 2022, A&A, 657, A54
Bertaux J. L., Lallement R., Ferron S., Boonne C., Bodichon R., 2014, A&A,
   564, A46
Bettinelli M., Hidalgo S. L., Cassisi S., Aparicio A., Piotto G., 2018, MNRAS,
Bettinelli M., Hidalgo S. L., Cassisi S., Aparicio A., Piotto G., Valdes F., Walker
   A. R., 2019, MNRAS, 487, 5862
Bonifacio P., et al., 2024, A&A, 684, A91
Bono G., et al., 2020, A&A, 644, A96
Bothun G. D., Dressler A., 1986, ApJ, 301, 57
Bressan A., Marigo P., Girardi L., Salasnich B., Dal Cero C., Rubele S., Nanni
   A., 2012, MNRAS, 427, 127
Carrera R., Aparicio A., Martínez-Delgado D., Alonso-García J., 2002, AJ, 123,
   3199
Chen Y., et al., 2019, A&A, 632, A105
Christy R. F., 1966, ARA&A, 4, 353
Clementini G., et al., 2023, A&A, 674, A18
D'Souza R., Bell E. F., 2022, MNRAS, 512, 739
De Boer T. J. L., et al., 2011, A&A, 528, A119
De Boer T. J. L., et al., 2012a, A&A, 539, A103
De Boer T. J. L., et al., 2012b, A&A, 544, A73
De Boer T. J. L., Tolstoy E., Lemasle B., Saha A., Olszewski E. W., Mateo M.,
   Irwin M. J., Battaglia G., 2014, A&A, 572, A10
Dohm-Palmer R. C., et al., 1997, AJ, 114, 2527
Duquennoy A., Mayor M., 1991, A&A, 248, 485
Eskridge P. B., Schweitzer A. E., 2001, AJ, 122, 3106
```

Ferraro F. R., Paltrinieri B., Rood R. T., Dorman B., 1999, ApJ, 522, 983

```
Fiorentino G., Lanzoni B., Dalessandro E., Ferraro F. R., Bono G., Marconi M.,
   2014, ApJ, 783, 34
Fritz T. K., Carrera R., Battaglia G., Taibi S., 2019, A&A, 623, A129
Gallart C., Zoccali M., Aparicio A., 2005, ARA&A, 43, 387
Garrison-Kimmel S., Boylan-Kolchin M., Bullock J. S., Lee K., 2014, MNRAS,
Gott J. Richard I., 1975, ApJ, 201, 296
Grcevich J., Putman M. E., 2009, ApJ, 696, 385
Gullieuszik M., Held E. V., Rizzi L., Girardi L., Marigo P., Momany Y., 2008,
   MNRAS, 388, 1185
Hammer F., Puech M., Chemin L., Flores H., Lehnert M. D., 2007, ApJ, 662,
Hammer F., Yang Y., Wang J., Arenou F., Puech M., Flores H., Babusiaux C.,
   2019, ApJ, 883, 171
Hammer F., et al., 2023, MNRAS, 519, 5059
Hammer F., et al., 2024, MNRAS, 527, 2718
Hennebelle P., Brucy N., Colman T., 2024, arXiv e-prints, p. arXiv:2404.17368
Hidalgo S. L., et al., 2018, ApJ, 856, 125
Hill V., et al., 2019, A&A, 626, A15
Jiao Y., Hammer F., Wang H., Wang J., Amram P., Chemin L., Yang Y., 2023,
   A&A, 678, A208
Kallivayalil N., van der Marel R. P., Besla G., Anderson J., Alcock C., 2013,
   ApJ, 764, 161
Kinemuchi K., Harris H. C., Smith H. A., Silbermann N. A., Snyder L. A., La
   Cluyzé A. P., Clark C. L., 2008, AJ, 136, 1921
Kirby E. N., Lanfranchi G. A., Simon J. D., Cohen J. G., Guhathakurta P., 2011,
   ApJ, 727, 78
Koch A., Grebel E. K., Wyse R. F. G., Kleyna J. T., Wilkinson M. I., Harbeck
   D. R., Gilmore G. F., Evans N. W., 2006, AJ, 131, 895
Komiyama Y., et al., 2007, AJ, 134, 835
Kroupa P., 2001, MNRAS, 322, 231
Lee M. G., Yuk I.-S., Park H. S., Harris J., Zaritsky D., 2009, ApJ, 703, 692
Li H., Hammer F., Babusiaux C., Pawlowski M. S., Yang Y., Arenou F., Du C.,
   Wang J., 2021, ApJ, 916, 8
Lombardo L., et al., 2021, A&A, 656, A155
Mapelli M., Ripamonti E., Tolstoy E., Sigurdsson S., Irwin M. J., Battaglia G.,
   2007, MNRAS, 380, 1127
Mapelli M., Ripamonti E., Battaglia G., Tolstoy E., Irwin M. J., Moore B., Sig-
   urdsson S., 2009, MNRAS, 396, 177
Maran S. P., 1991, The Astronomy and Astrophysics Encyclopedia. Wiley
Martin N. F., et al., 2008, ApJ, 672, L13
Mashonkina L., Jablonka P., Pakhomov Y., Sitnova T., North P., 2017, A&A,
   604, A129
Mateo M., Hurley-Keller D., Nemec J., 1998, AJ, 115, 1856
Matteucci F., Recchi S., 2001, ApJ, 558, 351
Mayer L., Mastropietro C., Wadsley J., Stadel J., Moore B., 2006, MNRAS, 369,
McConnachie A. W., Venn K. A., 2020, AJ, 160, 124
Meyer F., Meyer-Hofmeister E., 1980, in Plavec M. J., Popper D. M., Ulrich
   R. K., eds, Vol. 88, Close Binary Stars: Observations and Interpretation. pp
Milone A. A. E., Latham D. W., Mathieu R. D., Morse J. A., Davis R. J., 1992,
   in Kondo Y., Sistero R., Polidan R. S., eds, Vol. 151, Evolutionary Processes
   in Interacting Binary Stars. p. 473
Momany Y., Held E. V., Saviane I., Zaggia S., Rizzi L., Gullieuszik M., 2007,
   A&A, 468, 973
Monelli M., Fiorentino G., 2022, Universe, 8, 191
Monelli M., et al., 2003, AJ, 126, 218
Muñoz R. R., Côté P., Santana F. A., Geha M., Simon J. D., Oyarzún G. A.,
   Stetson P. B., Djorgovski S. G., 2018, ApJ, 860, 66
Ou X., Eilers A.-C., Necib L., Frebel A., 2024, MNRAS, 528, 693
Pace A. B., Li T. S., 2019, ApJ, 875, 77
Perets H. B., Fabrycky D. C., 2009, ApJ, 697, 1048
Pietrinferni A., et al., 2021, ApJ, 908, 102
Pietrinferni A., Salaris M., Cassisi S., Savino A., Mucciarelli A., Hyder D., Hi-
   dalgo S., 2024, MNRAS, 527, 2065
Putman M. E., Zheng Y., Price-Whelan A. M., Grcevich J., Johnson A. C.,
   Tollerud E., Peek J. E. G., 2021, ApJ, 913, 53
Raso S., et al., 2019, ApJ, 879, 56
Riello M., et al., 2021, A&A, 649, A3
Ripepi V., Molinaro R., Musella I., Marconi M., Leccia S., Eyer L., 2019, A&A,
   625, A14
Robin A. C., et al., 2012, A&A, 543, A100
Rocha M., Peter A. H. G., Bullock J., 2012, MNRAS, 425, 231
Rossi M., Salvadori S., Skúladóttir Á., 2021, MNRAS, 503, 6026
```

Ruiz-Lara T., et al., 2021, MNRAS, 501, 3962

Cassisi S., 2021, MNRAS, 502, 642

Rusakov V., Monelli M., Gallart C., Fritz T. K., Ruiz-Lara T., Bernard E. J.,

```
Saffer R. A., Sepinski J. F., De Marchi G., Livio M., Paresce F., Shara M. M.,
   Zurek D., 2002, in Shara M. M., ed., Astronomical Society of the Pacific Con-
   ference Series Vol. 263, Stellar Collisions, Mergers and their Consequences.
   p. 157
Santana F. A., Muñoz R. R., Geha M., Côté P., Stetson P., Simon J. D., Djorgov-
   ski S. G., 2013, ApJ, 774, 106
Santistevan I. B., Wetzel A., Tollerud E., Sanderson R. E., Samuel J., 2023, MN-
   RAS, 518, 1427
Saviane I., Held E. V., Bertelli G., 2000, A&A, 355, 56
Sbordone L., Caffau E., Bonifacio P., Duffau S., 2014, A&A, 564, A109
Schlegel D. J., Finkbeiner D. P., Davis M., 1998, ApJ, 500, 525
Sestito F., et al., 2023, MNRAS, 525, 2875
Shara M. M., Saffer R. A., Livio M., 1997, ApJ, 489, L59
Sigurdsson S., Phinney E. S., 1995, ApJS, 99, 609
Sills A., Karakas A., Lattanzio J., 2009, ApJ, 692, 1411
Soszyński I., et al., 2020, ApJ, 901, L25
Starkenburg E., et al., 2010, A&A, 513, A34
Stetson P. B., Hesser J. E., Smecker-Hane T. A., 1998, PASP, 110, 533
Tolstoy E., Hill V., Tosi M., 2009, ARA&A, 47, 371
Tolstoy E., et al., 2023, A&A, 675, A49
Toonen S., Boekholt T. C. N., Portegies Zwart S., 2022, A&A, 661, A61
Wang J., Hammer F., Yang Y., Pawlowski M. S., Mamon G. A., Wang H., 2024,
   MNRAS, 527, 7144
Weisz D. R., Dolphin A. E., Skillman E. D., Holtzman J., Gilbert K. M., Dalcan-
   ton J. J., Williams B. F., 2014, ApJ, 789, 147
Yang Y., Hammer F., Fouquet S., Flores H., Puech M., Pawlowski M. S., Kroupa
   P., 2014, MNRAS, 442, 2419
Yang Y., Hammer F., Jiao Y., Pawlowski M. S., 2022, MNRAS, 512, 4171
```

Zhu J., Tonnesen S., Bryan G. L., 2024, ApJ, 960, 54

Appendix A: Detection of CHeBs in other dSphs

For Draco, UMi, and Sextans dSphs, the methodology to derive CHeB counts is very similar to that described for Sculptor (see Sect. 3). The precise locations of the 2-Gyr limit of RGB are different for each dSphs because we computed the corresponding evolutionary tracks according to their Galactic extinctions, respectively. The detection of CHeBs in each dSphs are described by Figure A.1, and their stellar parameters are shown in Figure A.2. A special remark for UMI: following the algorithm of defining the $r_{\rm ell}$ in Sect. 3.3.2, we found a relative large value of $r_{\rm ell} = 2.5$ deg, which is possibly related to the extended stellar halo by Sestito et al. (2023). Nonetheless, we choose to fix $r_{\rm ell} = 1.48$ deg, i.e., $5r_{\rm half}$, to deduce the statistics in Table 2, in order to keep consistency with the analysis of other dwarf galaxies.

However, Gaia data are insufficiently deep to properly detect the CHeB population in Fornax and Carina. Fornax is located at 141 kpc, i.e., a distant module $m-M_0=20.72$, i.e., one magnitude fainter than Sculptor. Thus, when applying our selection of CHeB candidate, the faint limit (G=20.65) of our CHeB condition in Fornax is too close to the limiting magnitude of Gaia, G=20.8 as we have adopted. Then, "Gaia" CHeB candidates in Fornax are likely contaminated by RGB or AGB stars because the photometric errors in color are likely too large. The only way to solve this problem is to replace the Gaia photometric data by more accurate data. DES is a good choice because it provides not only a high quality photometry but also a wide coverage on sky.

We retrieved a catalog of sources from the DES data release 2 (DR2) within 2.5-degree radius centered on Fornax, using |extended_class_coadd|<=1, as recommended by the DES-DR2 official document⁸. To combine the DES and *Gaia* data, we cross-matched the *Gaia* PM-selected sample of Fornax to the DES star catalog, and obtained a "GaiaPM-DES" catalog, which is based on the DES photometry, and for which the MW huge contamination has been filtered by the *Gaia* PMs.

To select CHeB candidate, we have transformed the CHeB selection condition that is defined in *Gaia* photometric system into the DES photometric system, using the photometric relationships provided by *Gaia* EDR3 (Sect. 5.5.1 in "*Gaia* early data release 3 documentation"):

$$G - g = 0.2199 - 0.6365 x - 0.1548 x^2 + 0.0064 x^3$$
, (A.1)

 $G - i = -0.293 + 0.6404 \, x - 0.09609 \, x^2$

$$-0.002104 x^3$$
, (A.2)

 $G - r = -0.09837 + 0.08592 \, x - 0.1907 \, x^2 - 0.1701 \, x^3$

$$+0.02263 x^4$$
, (A.3)

where $x = G_{BP} - G_{RP}$. The CHeB selection condition in DES photometric system is shown by the red-dashed line in Figure A.1, where the Fornax' CHeB candidates are indicated by blue dots.

For Carina, we have similar difficulties as in Fornax based on only the *Gaia* data, due to its relative large distance of 106 kpc ($m - M_0 = 20.13$). Because Carina is not covered by DES, we have to adopt the observation from the MegaCam survey by Muñoz et al. (2018), as an accurate photometric alternative. The MegaCam observation on Carina covers $0^{\circ}7 \times 0^{\circ}7$, and was carried out using the MegaCam at the Canada France Hawaii Telescope (CFHT), which adopted a slightly different filter system

than DES. In order to apply the same CHeB selection to Mega-Cam filters, we have translated the selection line from Gaia's photometric system into that of DES (using Eqs. A.1 and A.3), then into MegaCam photometric systems, i.e., g' and r' by applying the other two formula below⁹:

$$g' = g - 0.153(g - r), (A.4)$$

$$r' = r - 0.024(g - r). \tag{A.5}$$

Then, we cross-matched the MegaCam catalog with Carina's *Gaia* PM-selected sample to obtain a "GaiaPM-MegaCam" catalog, and finally obtained the GaiaPM-MegaCam CHeB candidates, as shown in Figure A.1.

After obtaining the CHeB Candidates of Carina and Fornax, we made the statistics on the candidates using the same methods described in Sect. 3.3, and the results are listed in Table 2. Note that, to derive the stellar parameters of CHeB candidates, we have generated the corresponding reddened PARSEC evolutionary tracks in DESCam and MegaCam systems that are dedicated to Fornax and Carina, respectively.

⁸ https://des.ncsa.illinois.edu/releases/dr2/dr2-faq

⁹ https://www.cadc-ccda.hia-iha.nrc-cnrc.gc.ca/en/
megapipe/docs/filtold.html

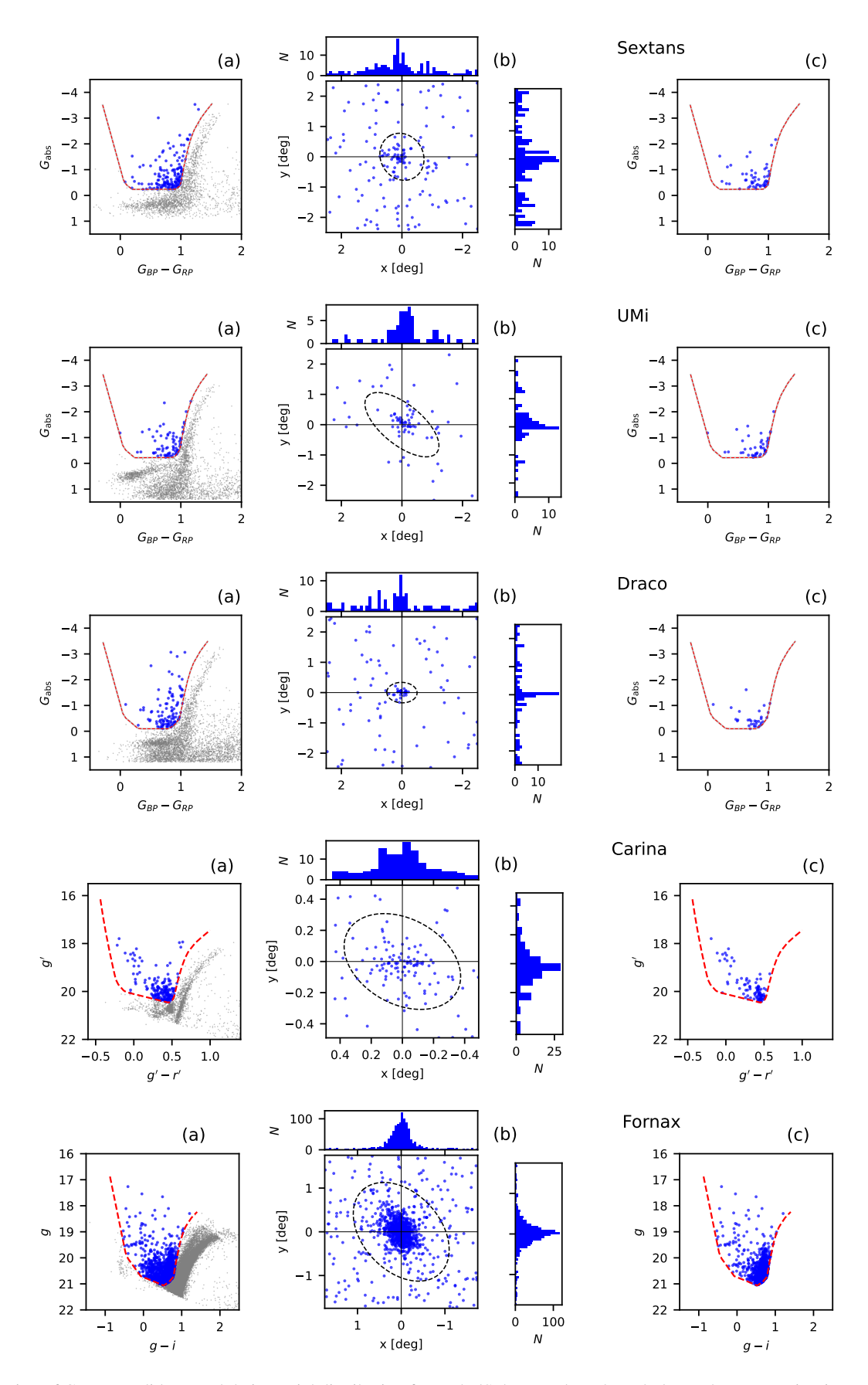


Fig. A.1. Selection of CHeB candidates and their spatial distribution for each dSphs. Panels and symbols are the same as in Figure 4.

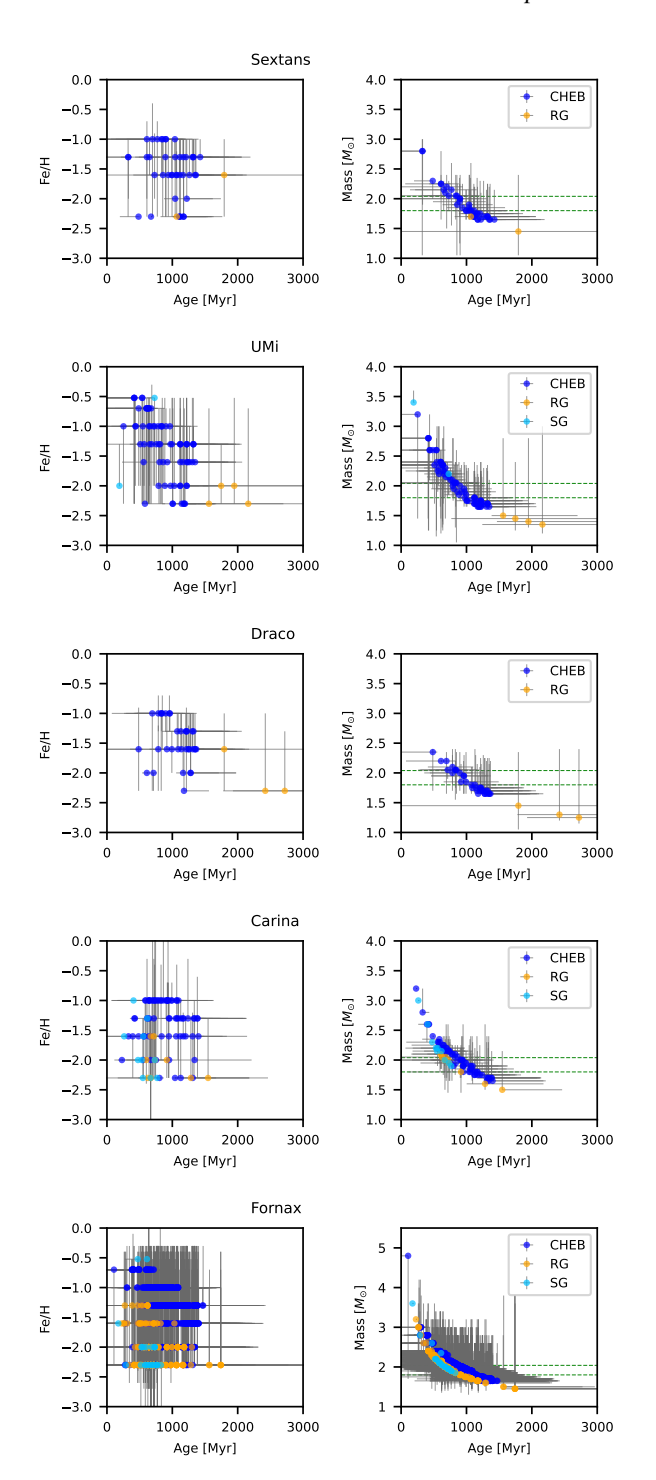


Fig. A.2. Age-metallicity (*Left*) and age-mass (*Right*) relations for CHeB stars in their different evolutionary phases (indicated by color explained in the legend) for each dSph, respectively. The two dashed lines in the right panel indicate the masses of 1.8, 2.04 M_{\odot} , respectively.

Appendix B: Solutions for stellar parameters

An evolutionary track of a star is initialized by a stellar mass and a metallicity (which is, of cause, simplified for our main interests), and is made of a sequence of points in time (i.e., age) that describe the corresponding parameters of the evolutionary track of the star. When we follow the latter in the CMD, it evolves at different speeds. For the i-th point of the track at time t^i , we may

calculate an evolutionary speed in both magnitude and color, as

$$v_{\text{mag}}^{i} = \frac{|m^{i+1} - m^{i-1}|}{t^{i+1} - t^{i-1}},$$
(B.1)

$$v_{\text{col}}^{i} = \frac{|c^{i+1} - c^{i-1}|}{t^{i+1} - t^{i-1}},$$
(B.2)

where $m = G_{abs}$ and $c = G_{BP} - G_{RP}$ in the *Gaia* photometric system. Assuming a track that is broadened by star photometric uncertainties $(m \pm \Delta m \text{ and } c \pm \Delta c)$, we may calculate the time that the track needs to pass through twice of the error bars, respectively, as

$$\tau_{\rm mag}^i = 2\,\Delta m/v_{\rm mag}^i,\tag{B.3}$$

$$\tau_{\rm col}^i = 2\,\Delta c/v_c^i,\tag{B.4}$$

Here, we adopted 1-sigma errors for Δm and Δc in magnitude and color, respectively, when working with Gaia photometry, while a "3 sigma error" was adopted when working on the DES and MegaCam dataset. The latter two datasets provide very accurate photometry, namely, small errors, while the grid of the PARSEC evolutionary track currently adopted is too large when compared to the small error bars obtained from both deep observations. Thus, we have to enlarge the searching window when looking for possible solutions in evolutionary tracks. In practice, the photometric errors for a given star could cover not only one or more points of the same track, but also cover one or more different evolutionary tracks. Our goal is to retrieve the most probable evolutionary track. Thus, we need to average all points of the same track that are covered by the photometric errors, by evaluating the mean au_{mag} and au_{col} of the points, together with the mean of the stellar parameters (see Table B.1 for example). The column N_{shot} tells the number of points of a track that is covered by the photometric errors. Taking the multiplication of $au_{
m mag} au_{
m col}$ as the final weighting, we sort tracks that are covered by Δm and Δc , and identify the most probable one with the maximal elapsed-time.

As the final solution for a given star, we report its most probable evolutionary track, together with the range of tracks that are indexed by stellar mass. In another words, we report the parameters of the tracks of minimal or maximal stellar mass. In doing this, we keep the physical consistency in between parameters. In the PARSEC library, evolution phases are normalized into a number p, ranging from 1 to 15, and each integer point corresponds to the starting of a new phase of the evolution. Our dictionary is 1 < p(PMS) < 5 < p(MS) < 6 < p(SG) < 8 < p(RGB) < 11 < p(CHeB) < 14 < p(AGB) < 15.

Table B.1. Examples of the estimation of stellar parameters

Example 1: A star in Sculptor: $G_{abs} = -0.7984 \pm 0.0013$, $G_{BP} - G_{RP} = 0.919 \pm 0.024$ Possible solutions:

- T	3.6	CD /TT1		DI	3.7			
Track	Mass	[Fe/H]	Age	Phase	$N_{ m shot}$	$ au_{ m mag}$	$ au_{ m col}$	$ au_{ m mag} au_{ m col}$
	M_{\odot}		(Myr)			(Myr)	(Myr)	(Myr^2)
1	2.25	-1.602	543.5	СНеВ	3	14.2	7.0	99.3
2	2.10	-1.000	830.5	СНеВ	1	0.289	6.5	1.87
3	2.15	-2.000	572.6	СНеВ	1	0.0858	9.0	0.776
4	2.05	-2.000	644.3	СНеВ	1	0.0632	11.0	0.717
5	2.35	-1.301	511.8	СНеВ	1	0.127	4.5	0.565
6	2.00	-2.301	670.1	RG	1	0.0103	2.8	0.0286
7	2.00	-2.000	687.5	СНеВ	1	0.00835	1.9	0.016
8	1.80	-1.602	1111.8	СНеВ	3	0.0297	0.39	0.0117
9	2.10	-2.301	587.3	RG	1	0.00774	1.5	0.0113
10	1.75	-1.602	1206.0	AG	1	0.00221	0.23	0.000514

Example 2: Astar in Sculptor: $G_{abs} = -0.5177 \pm 0.0016$, $G_{BP} - G_{RP} = 0.942 \pm 0.027$

	e solutio							
Track	Mass	[Fe/H]	Age	Phase	$N_{\rm shot}$	$ au_{ m mag}$	$ au_{ m col}$	$ au_{ m mag} au_{ m col}$
	M_{\odot}		(Myr)			(Myr)	(Myr)	(Myr^2)
1	1.40	-2.301	1916.1	RG	1	0.0641	14	0.882
2	1.55	-2.000	1415.4	RG	1	0.0499	11	0.573
3	1.95	-2.000	738.7	СНеВ	1	0.0578	9.6	0.558
4	1.55	-2.301	1399.5	RG	1	0.0499	11	0.549
5	1.60	-2.301	1271.5	RG	1	0.0454	9.9	0.448
6	2.35	-1.000	536.1	СНеВ	1	0.0835	4.5	0.374
7	1.65	-2.000	1176.5	RG	1	0.04	7.8	0.31
8	2.05	-1.301	709.8	СНеВ	1	0.0404	5.9	0.237
9	1.50	-2.000	1563.7	RG	1	0.0416	4.3	0.177
10	1.85	-2.000	847.6	RG	1	0.0172	4.2	0.0719
11	1.85	-1.602	883.0	RG	1	0.0152	2.9	0.0437
12	1.75	-1.301	1272.8	СНеВ	1	0.0263	1.1	0.0285
13	1.95	-1.602	765.3	RG	1	0.0116	2.1	0.0246
14	1.70	-1.301	1386.2	CHeB	1	0.0134	0.81	0.0109
15	2.10	-1.301	658.1	RG	1	0.00837	1.2	0.0102
16	2.10	-1.602	629.3	RG	1	0.00813	1.1	0.0093
17	2.15	-1.602	592.0	RG	1	0.0067	0.99	0.00667
18	2.20	-1.301	583.2	RG	1	0.00672	0.93	0.00623

Example 3: A star in UMi: $G_{abs} = -2.3467 \pm 0.0009$, $G_{BP} - G_{RP} = 0.728 \pm 0.010$ Possible solutions:

Track	Mass	[Fe/H]	Age	Phase	$N_{ m shot}$	$ au_{ m mag}$	$ au_{ m col}$	$ au_{ m mag} au_{ m col}$
	M_{\odot}		(Myr)			(Myr)	(Myr)	(Myr^2)
1	3.40	-2.000	190.7	SG	1	0.000582	0.0025	1.45e-06
2	3.60	-1.301	179.3	SG	1	0.000468	0.0023	1.09e-06

Example 4: A star in Draco: $G_{abs} = -0.3985 \pm 0.0127$, $G_{BP} - G_{RP} = 0.487 \pm 0.067$

1 055101	e solutio	115.						
Track	Mass	[Fe/H]	Age	Phase	$N_{ m shot}$	$ au_{ m mag}$	$ au_{ m col}$	$ au_{ m mag} au_{ m col}$
	M_{\odot}		(Myr)			(Myr)	(Myr)	(Myr^2)
1	1.70	-2.000	1164.5	СНеВ	6	4.2	51	214
2	1.65	-2.000	1270.8	CHeB	13	4.37	47	203
3	1.80	-2.301	941.1	CHeB	4	2.87	6.3	18.1
4	1.85	-2.000	885.8	CHeB	2	1.91	4.3	8.16
5	2.00	-2.301	666.9	SG	8	0.286	0.24	0.0694
6	2.15	-1.301	617.3	SG	1	0.136	0.21	0.0287

Appendix C: BSS formed from the fusion of a triple system

The CHeB stars can be used to determine star formation histories (see e.g., Dohm-Palmer et al. 1997), having the advantage to be brighter than MS stars. The presence of a CHeB vertical sequence is usually taken as evidence of the presence of a young population. However, as pointed out by Momany et al. (2007), this can be ambiguous, and they quote as example the

GC M 80, for which Ferraro et al. (1999) detected a population of CHeB stars. Since a recent star formation in an old GC can be ruled out, these stars have to be interpreted as evolved BSSs. The BSSs population is very developed in M 80 and can explain the presence of evolved BSSs. We point out that a crucial quantity is the masses of the CHeB stars. The brightest CHeB stars in M 80 are brighter than the HB, however their mass is of the order of $1.8 \, M_{\odot}$. Such a mass is compatible with the merging of two $0.9 \, M_{\odot}$ stars. The fainter stars in the CHeB sequence of

M 80 have lower masses. While for masses lower than $1.8 M_{\odot}$ a CHeB could be either a young star or a BSSs, for larger masses the BSS explanation requires the merging of at least three stars.

The formation of a BSS by the fusion of three stars requires the evolution of a triple system through a common envelope phase (Meyer & Meyer-Hofmeister 1980). Measurements of BSS masses are rare in the literature (see e.g. Raso et al. 2019, and references therein). In the globular cluster 47 Tuc (= NGC 104, metallicity around -0.7), Raso et al. (2019) could measure masses for 23 BSSs, of these, five have masses that are formally larger than twice the turnoff mass of the cluster. However the errors are large enough that they are all consistent with being below this limit. If all the five stars were truly with masses above twice the turnoff mass, this would give a fraction of 22% of BSSs descendants from triple systems. Inspection of figure 8 of Raso et al. (2019) suggest that only one star, BSS1, is marginally consistent with a mass slightly larger than twice the turnoff mass. In this case the fraction of descendants from triple systems would be $1/23 \sim 4\%$. Shara et al. (1997) measured the mass of a BSS in 47Tuc and found 1.7±0.4 M_o. They argue that the most likely path for formation of this star is the (slow) coalescence of a binary formed by two stars of nearly $0.9\,\mathrm{M}_\odot$ each. Fiorentino et al. (2014) have studied the pulsational masses of BSSs in the Globular Cluster NGC 6541 (metallicity of -1.76, age= 13.25 Gyr). They found BSSs in the mass range 1.0–1.1 M_{\odot} , in agreement with masses deduced from evolutionary tracks of single stars.

To get some further insight on the fraction of triple systems we decided to look at the Gaia Universe Model (herefater GUM, Robin et al. 2012)¹⁰. The binary frequency and how this is folded into GUM is discussed by Arenou (2011). The fraction of triple systems among solar type stars is assumed to be 8.4% based on the results of Duquennoy & Mayor (1991). We selected from GUM stars with absolute magnitudes $M_G > 6$, metallicities [Fe/H] < 0 and Population > 1, that amounts to exclude disc stars. From the color-magnitude we selected the turnoff stars and found a fraction of binary systems of 31%, and 6% of triple systems. The latter value is not too different from the 4% that we estimated above for the BSSs descendants from triple systems in 47 Tuc. The fraction of triple systems is an upper limit to the fraction of the systems that can be progenitors of a BSSs of large mass. We must assume the system is hierarchical, otherwise it is unstable. We also assume the system has an inner couple, that at some stage undergoes a common envelope phase. In order for the outer third star, to be dragged into this common envelope and give rise to the fusion of the three stars the outer semi-major axis must be smaller or equal to the radius of the common envelope. From the above considerations, both from observations and from GUM we conclude that this channel of formation of BSS cannot exceed a few percent of the BSS population and is unlikely to explain their observed number.

In any case it is not only the fraction of triples that needs to be taken into account, but the fraction of triples that can result in a triple merger. On this the theoretical study of Toonen et al. (2022) is illuminating, since it shows that the collision of the inner couple in a destabilised triple system occurs in 13%–24% of

the cases, only for 2.4% of these the tertiary star may also collide resulting in a fusion of the three stars. We defer the reader on the discussion on this point in Bonifacio et al. (2024) who conclude, factoring all possible events, that at most 0.3% of the BSS may result from the fusion of three stars. This is not in contradiction with the suggestion of Perets & Fabrycky (2009) that triple systems are one of the main channels for the formation of BSS. In fact they envisage only the fusion of the inner couple, with mass less than or equal to twice the TO mass, with the tertiary remaining as companion of the BSS. This could explain the large fraction of long-period binaries among BSS.

¹⁰ The Gaia Universe Model is available through the Gaia archive (https://gea.esac.esa.int/archive/) and the relevant documentation can be found at https://gea.esac.esa.int/archive/ documentation/GDR3/Data_processing/chap_cu2sim/sec_ cu2UM/